Journal of Computational Physics 513 (2024) 113197

Contents lists available at ScienceDirect

Journal of Computational Physics

journal homepage: www.elsevier.com/locate/jcp

A novel approach to the characteristic splitting scheme for mildly compressible flows based on the weighted averaged flux method

A. Fiolitakis *, M. Pries

German Aerospace Centre, Paffenwaldring 38-40, Stuttgart, 70569, Germany

ARTICLE INFO

Keywords:
Characteristic splitting
Non-conservative hyperbolic system
Weighted averaged flux method
Implicit monotone scheme
Unstructured grid
Mildly compressible flows

ABSTRACT

In the present work we improve the characteristic splitting approach for computing mildly compressible flows. This splitting approach is consisted of two separate steps namely an advective step and a purely hyperbolic, acoustic step. Typically, a pressure correction method is used for solving the acoustic step which may lead to overly dispersive, incorrect results. As a remedy to this issue, a novel solution approach on the basis of the weighted averaged flux method (WAF) is proposed, which solves the non-conservative, hyperbolic equations of the acoustic step directly. The stability and accuracy of this novel WAF method is demonstrated and an implicit, monotone formulation for three-dimensional unstructured grids is given. The simulation of the non-reacting flow in a swirl burner proves the applicability of the method.

1. Introduction

The present work focuses on the characteristic splitting of [1] which is a numerical approach for the computation of mildly compressible flows. The key idea of this approach is to derive a numerical splitting scheme by decomposing the Eigenvalues of the convective flux term's Jacobian matrix into flow velocity and the speed of sound. In this way a two step scheme is obtained which consists of an advective step followed by an acoustic step. The advantage of this approach is that for low Mach numbers the stiffness of the compressible flow equations (which is caused by the difference between the magnitude of flow velocity and speed of sound, cf. for example [2]) is eliminated. Each step of the scheme can be solved theoretically by a semi implicit scheme [1] (thus avoiding computationally expensive iterations), which makes the method particularly interesting for unsteady flow simulations like large-eddy simulations (LES). Since its introduction, the approach has therefore enjoyed an extensive usage in various fields like simulation of combustion instabilities in gas [3,4] and spray flames [5–8], various reactive flow simulations [9–20], simulations of combustion noise in conjunction with computational aero acoustics [21–23], droplet vaporization [24], flame wall interaction [25,26], fluid structure interaction [27,28] and even simulations of environmental problems [29,30]. A recent extension of the scheme includes real gas effects [31]. Improvements on this scheme are presented in [32] where total energy is used as an energy variable and simplifications to the pressure correction equation are proposed which increase the stability of the scheme. In [32] an iterative advective step is also suggested for multi-species flows in order to increase the accuracy. The differences between the scheme of [1] and [32] are illustrated in Fig. 1. The approach of [32] is termed "implicit characteristic splitting" (ICS) to distinguish it from [1]. This ICS scheme is the focal point of the present work. It is found that despite the improvements in [32], problems may occur in the simulation of standing pressure waves where large dispersive errors render the numerical solution useless (similar observations are

* Corresponding author.
E-mail address: andreas.fiolitakis@dlr.de (A. Fiolitakis).

https://doi.org/10.1016/j.jcp.2024.113197
Received 17 August 2023; Received in revised form 7 May 2024; Accepted 9 June 2024

Available online 13 June 2024

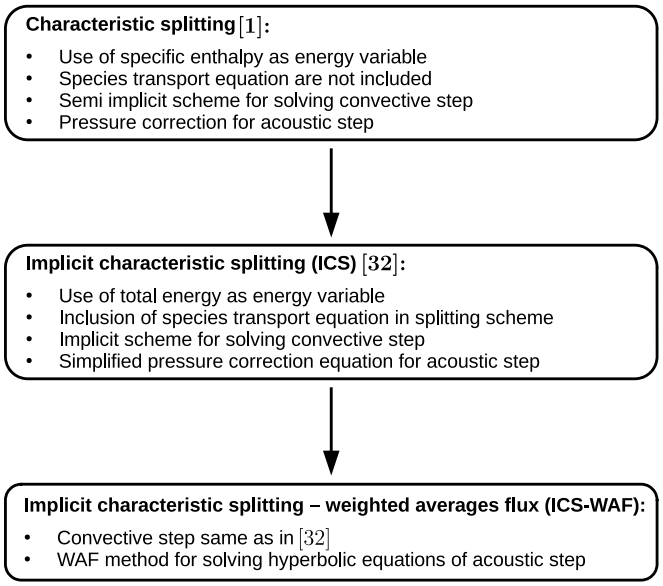

Fig. 1. Overview of the different numerical schemes based on characteristic splitting.

also reported in [33] where standing pressure waves are computed with various density based solvers). The root of this problem lies in the pressure correction equation which is used in [32] (and also in [1] where the pressure correction equation is initially introduced) for computing pressure in the acoustic step of the ICS scheme. This pressure correction equations utilizes a purely central, second order spatial discretization which does not ensure monotonicity of the solution. The main objective of the present work is therefore to find a solution for this problem by deriving a new, monotone numerical scheme for solving the hyperbolic equations of the acoustic step. We build this solution method on the weighted averaged flux (WAF) scheme [34] since the equations for the acoustic step are non-conservative. The changes made to the ICS scheme are illustrated in Fig. 1 where the new scheme is termed ICS-WAF method. The outline of this ICS-WAF method for three-dimensional unstructured meshes is given in Sec. 2 where also a von Neumann stability analysis [35,36] of the overall splitting scheme is provided. The accuracy of the method and its applicability to practical problems is discussed in Sec. 3.

It should be stressed at this point that the characteristic splitting is not the only method available for computing mildly compressible flows. Similar approaches which avoid the stiffness at low Mach numbers by using a splitting approach are provided in [37–50]. For low Mach number and all speed flows the flux-vector splitting scheme introduced in [51,52] forms the basis of several numerical methods. In addition, preconditioned density based schemes enjoy an extensive use for computing low Mach number flows. An overview on established approaches such as [53–57] is given in [58]. Other examples involve [59] where a preconditioning matrix for all speeds is proposed as well as [60] where a preconditioner in diagonal form for arbitrary Mach numbers is derived. In [61] a preconditioning is presented which is capable of handling the stiffness due to low Mach number as well as the stiffness caused by high-aspect ratio cells. An improved control of the preconditioning for viscosity dominated flows is discussed in [62]. A preconditioning which targets distinct physics separately is introduced in [63]. In [64] a low Mach number fix for the Roe scheme is presented. Based on an asymptotic analysis the Harten-Lax-van Leer (HLL) scheme is extended to low Mach number flows in [65]. The HLL algorithm is also used in [66] in conjunction with the splitting given in [51]. Methods given in [67,68] are also based on the splitting scheme of [51]. With the help of an artificial dissipation term a density based scheme is applied to low Mach number flow regimes in [69]. For multi-phase flows at all Mach numbers a hybrid advection upstream splitting method is introduced in [70]. An approach presented in [71] is based on a Suliciu relaxation type to compute weak solutions of the Euler equations at all Mach numbers. By using the entropy inequality in place of the total energy conservation law a thermodynamically compatible finite volume scheme is derived in [72]. Density based schemes are also used in conjunction with discontinuous Galerkin method to compute flows over a wide range of Mach numbers, e.g. [73–84]. For the computation of low Mach numbers flows the discontinuous Galerkin discretization in space is frequently combined with an implicit/explicit (IMEX) time discretization [85–89]. Further use of IMEX time discretization for all speed flows and low Mach number flows may be found in [90–105] where the main focus is on the solution of the Euler equations and in [106–109]. In addition to density based methods pressure based methods may also be used for computing compressible flows, cf. [110–136] and [137–142] where multiple pressure variables are utilized. The solution of the Euler equations at all speeds by using implicit and semi implicit schemes in primitive variables is described in [143,144]. In [145] a semi implicit pressure based method for solving the Navier-Stokes equations with general equations of state is presented which is extended in [146] to high order of accuracy by using a discontinuous Galerkin scheme. Semi implicit pressure based schemes are also proposed in [147] (a space-time discontinuous Galerkin method is utilized here), [148] (in conjunction with an IMEX scheme for time integration), and in [149] (where a structure-preserving staggered scheme is introduced). Weakly compressible flows are also investigated in a pressure based framework by means of the finite element [150] and discontinuous Galerkin method [151].

Solution methods utilizing hybrid finite volume/finite element discretization are described in [152–154]. Pressure based methods are also extended to the computation of compressible and mildly compressible two- and multi-phase flows, e.g. [155–158]. Despite these various alternative approaches the characteristic splitting still merits further improvements given its relevance in various fields.

2. Methodology

2.1. Overview of the basic splitting scheme

We are interested in solving the balance equations for mass, momentum and energy together with the transport equations for species. These equations are given by (Einstein notation)

$$\frac{\partial \rho}{\partial t} + \frac{\partial \rho u_i}{\partial x_i} = 0 \tag{1}$$

$$\frac{\partial \rho u_j}{\partial t} + \frac{\partial \rho u_i u_j}{\partial x_i} = -\frac{\partial p}{\partial x_j} + \frac{\partial \tau_{ij}}{\partial x_i} \tag{2}$$

$$\frac{\partial \rho E}{\partial t} + \frac{\partial}{\partial x_i}\left(\rho u_i \left(E + \frac{p}{\rho}\right)\right) = \frac{\partial u_j \tau_{ij}}{\partial x_i} - \frac{\partial q_i}{\partial x_i} \tag{3}$$

$$\frac{\partial \rho Y_\alpha}{\partial t} + \frac{\partial \rho u_i Y_\alpha}{\partial x_i} = -\frac{\partial j_{i\alpha}}{\partial x_i} + S_\alpha \ . \tag{4}$$

Here t is the time, x_i the spatial coordinate, ρ the density, p the pressure, u_i the ith component of the velocity vector, Y_α the mass fraction of the species α (there are a total of $N_s - 1$ linearly independent species, where N_s is the total number of species), and E the total energy. τ_{ij} is the ij component of the viscous stress tensor, q_i the ith component of the vector of the diffusive heat flux and $j_{i\alpha}$ and S_α the ith component of the diffusive mass flux vector and chemical source term of the species α, respectively. It is assumed that the fluid is a mixture of thermally perfect gases and that the equation of state is given by the ideal gas law. The characteristic based splitting [1] is based on a decomposition of the Eigenvalues associated with the convective flux terms into the flow velocity and the speed of sound. As outlined in [32] we obtain the Equations (Einstein notation)

$$\frac{\partial \rho}{\partial t} + \frac{\partial \rho u_i}{\partial x_i} - \rho \frac{\partial u_i}{\partial x_i} = 0 \tag{5}$$

$$\frac{\partial \rho u_j}{\partial t} + \frac{\partial \rho u_i u_j}{\partial x_i} - \rho u_j \frac{\partial u_i}{\partial x_i} = \frac{\partial \tau_{ij}}{\partial x_i} \tag{6}$$

$$\frac{\partial \rho E}{\partial t} + \frac{\partial \rho u_i E}{\partial x_i} - \rho E \frac{\partial u_i}{\partial x_i} = \frac{\partial u_j \tau_{ij}}{\partial x_i} - \frac{\partial q_i}{\partial x_i} \tag{7}$$

$$\frac{\partial \rho Y_\alpha}{\partial t} + \frac{\partial \rho u_i Y_\alpha}{\partial x_i} - \rho Y_\alpha \frac{\partial u_i}{\partial x_i} = -\frac{\partial j_{i\alpha}}{\partial x_i} + S_\alpha \tag{8}$$

for the advective step (where the solution is advanced from a time level n to an intermediate time level $\star$) and (Einstein notation)

$$\frac{\partial \rho}{\partial t} + \rho \frac{\partial u_i}{\partial x_i} = 0 \tag{9}$$

$$\frac{\partial \rho u_j}{\partial t} + \rho u_j \frac{\partial u_i}{\partial x_i} + \frac{\partial p}{\partial x_j} = 0 \tag{10}$$

$$\frac{\partial \rho E}{\partial t} + \rho E \frac{\partial u_i}{\partial x_i} + \frac{\partial u_i p}{\partial x_i} = 0 \tag{11}$$

$$\frac{\partial \rho Y_\alpha}{\partial t} + \rho Y_\alpha \frac{\partial u_i}{\partial x_i} = 0 \tag{12}$$

for the acoustic step (i.e. for the advancement of the solution from the intermediate time level $\star$ to the time level $n+1$). The ideal gas law remains valid within each step of the splitting. The equations of the acoustic step can be transformed further into (Einstein notation)

$$\frac{\partial p}{\partial t} + \rho c^2 \frac{\partial u_i}{\partial x_i} = 0 \tag{13}$$

$$\frac{\partial u_j}{\partial t} + \frac{1}{\rho}\frac{\partial p}{\partial x_j} = 0 \tag{14}$$

$$\frac{\partial s}{\partial t} = 0 \tag{15}$$

$$\frac{\partial Y_\alpha}{\partial t} = 0 \tag{16}$$

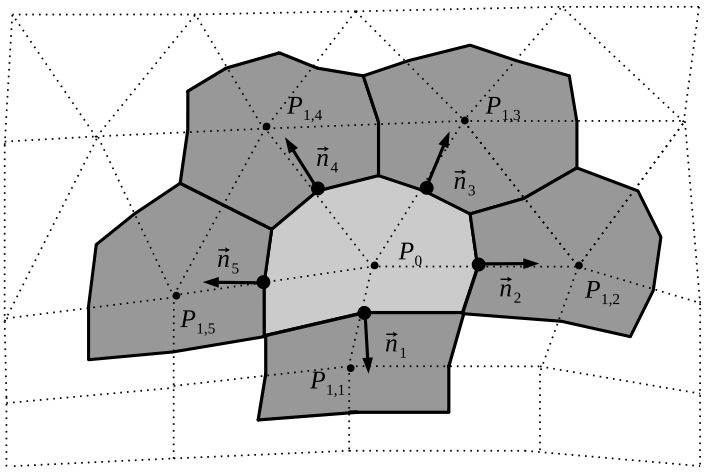

Fig. 2. A control volume P_0 of the dualgrid and its neighbors.

where c denotes the isentropic speed of sound. Note, that the specific entropy s and the composition Y_α remain constant over time during the acoustic step. They may, however, vary in space. The main objective of this work is to provide an alternate numerical scheme for solving the non-conservative hyperbolic Eqs. (13) and (14) under the constraints given by Eqs. (15) and (16).

2.2. The weighted averaged flux scheme for the acoustic step

A major difficulty in solving non-conservative hyperbolic equations such as Eqs. (13) and (14) is the definition of weak solutions in situations where discontinuities like shock waves are present. The problem stems from the fact that for non-conservative hyperbolic equations there is usually no Rankine-Hugoniot relation available to relate states across a discontinuity. One way of solving this problem is to introduce a general Rankine-Hugoniot relation which applies along a given family of paths in phase space [159]. This path definition forms the basis of the so called path conservative schemes, cf. [160]. It is found, however, that even these schemes may give incorrect results if strong discontinuities are present [161]. In this work we are primarily interested in smooth solutions which do not involve strong discontinuities (e.g. flows in gas turbine combustors). In [162] it is pointed out that non-conservative equations are adequate to capture physics under these conditions and the WAF scheme [34] is suggested as a suitable numerical approach for solving non-conservative hyperbolic equations. Therefore, the application of the WAF scheme to Eqs. (13) and (14) is outlined in the following. To this end Eqs. (13) and (14) are rewritten in terms of the vector $\vec{Q}$ and the coefficient matrices $\underline{\underline{A}}$, $\underline{\underline{B}}$ and $\underline{\underline{C}}$ as

$$\frac{\partial \vec{Q}}{\partial t} + \underline{\underline{A}} \frac{\partial \vec{Q}}{\partial x_1} + \underline{\underline{B}} \frac{\partial \vec{Q}}{\partial x_2} + \underline{\underline{C}} \frac{\partial \vec{Q}}{\partial x_3} = \vec{0} \tag{17}$$

$$\vec{Q} = \begin{pmatrix} p \\ u_1 \\ u_2 \\ u_3 \end{pmatrix} \qquad \underline{\underline{A}} = \begin{pmatrix} 0 & \rho c^2 & 0 & 0 \\ \rho^{-1} & 0 & 0 & 0 \\ 0 & 0 & 0 & 0 \\ 0 & 0 & 0 & 0 \end{pmatrix}$$

$$\underline{\underline{B}} = \begin{pmatrix} 0 & 0 & \rho c^2 & 0 \\ 0 & 0 & 0 & 0 \\ \rho^{-1} & 0 & 0 & 0 \\ 0 & 0 & 0 & 0 \end{pmatrix} \qquad \underline{\underline{C}} = \begin{pmatrix} 0 & 0 & 0 & \rho c^2 \\ 0 & 0 & 0 & 0 \\ 0 & 0 & 0 & 0 \\ \rho^{-1} & 0 & 0 & 0 \end{pmatrix} .$$

We seek to solve this system of equations on an unstructured median-dual mesh (these meshes are used by the in-house solver ThetaCOM [163] where this method is implemented). An example of such a mesh is shown in Fig. 2 where a control volume at the point P_0 is shown along with its neighboring control volumes $P_{1,f}$ (f denotes the face index). A finite volume discretization of Eq. (17) in P_0 is derived by using Gauss's theorem to determine the gradients, i.e.

$$\left.\frac{\partial \vec{Q}}{\partial x_i}\right|_{P_0} \approx \frac{1}{\Delta V_{P_0}} \sum_{f=1}^{N_{F,P_0}} \vec{Q}_f \, n_{i,f} \ ,$$

where N_{F,P_0} is the number of faces of the control volume located at P_0, $n_{i,f}$ is the ith component of face normal vector $\vec{n}_f$, ΔV_{P_0} the control volume's volume and $\vec{Q}_f$ the face value of $\vec{Q}$. We follow the approach given in [162] for non-conservative hyperbolic equations and obtain for Eq. (17) the discrete scheme

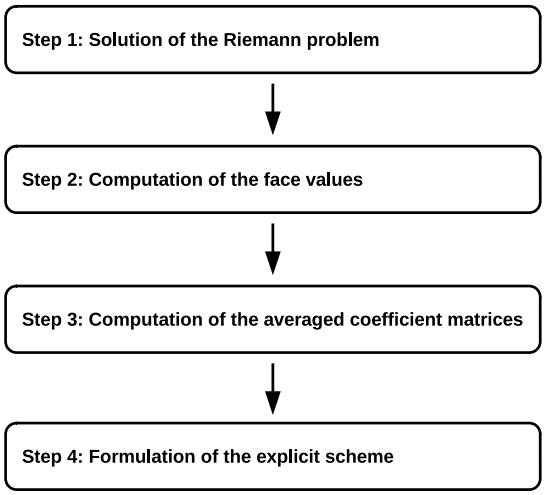

Fig. 3. Computational Steps of the WAF scheme.

$$\Delta V_{P_0}\,\frac{\vec{Q}^{n+1}-\vec{Q}^{\star}}{\Delta t}+\langle\underline{\underline{A}}\rangle_{P_0}\sum_{f=1}^{N_{F,P_0}}\vec{Q}_f^{\star+\frac{1}{2}}\,n_{1,f}+\langle\underline{\underline{B}}\rangle_{P_0}\sum_{f=1}^{N_{F,P_0}}\vec{Q}_f^{\star+\frac{1}{2}}\,n_{2,f}+\langle\underline{\underline{C}}\rangle_{P_0}\sum_{f=1}^{N_{F,P_0}}\vec{Q}_f^{\star+\frac{1}{2}}\,n_{3,f}=\vec{0} \tag{18}$$

$$\langle\underline{\underline{A}}\rangle_{P_0}=\begin{pmatrix}0 & \langle\rho\rangle_{P_0}\langle c^2\rangle_{P_0} & 0 & 0\\ \langle\rho\rangle_{P_0}^{-1} & 0 & 0 & 0\\ 0 & 0 & 0 & 0\\ 0 & 0 & 0 & 0\end{pmatrix}\quad \langle\underline{\underline{B}}\rangle_{P_0}=\begin{pmatrix}0 & 0 & \langle\rho\rangle_{P_0}\langle c^2\rangle_{P_0} & 0\\ 0 & 0 & 0 & 0\\ \langle\rho\rangle_{P_0}^{-1} & 0 & 0 & 0\\ 0 & 0 & 0 & 0\end{pmatrix}$$

$$\langle\underline{\underline{C}}\rangle_{P_0}=\begin{pmatrix}0 & 0 & 0 & \langle\rho\rangle_{P_0}\langle c^2\rangle_{P_0}\\ 0 & 0 & 0 & 0\\ 0 & 0 & 0 & 0\\ \langle\rho\rangle_{P_0}^{-1} & 0 & 0 & 0\end{pmatrix}.$$

Equation (18) is used for advancing the solution over a time step Δt from the intermediate time level $\star$ of the splitting scheme to the new time level $n+1$ ($\vec{Q}^{\star}$ and $\vec{Q}^{n+1}$ are the respective solution vectors at these time levels). $\vec{Q}_f^{\star+\frac{1}{2}}$ denotes face values which are determined on the basis of local Riemann problems at each face of the control volume. These Riemann problems also provide the basis for computing the averaged coefficient matrices $\langle\underline{\underline{A}}\rangle_{P_0}$, $\langle\underline{\underline{B}}\rangle_{P_0}$ and $\langle\underline{\underline{C}}\rangle_{P_0}$ which depend on the face average of density $\langle\rho\rangle_{P_0}$ and the face average of the square speed of sound $\langle c^2\rangle_{P_0}$. The individual steps required to obtain these values and to arrive at an explicit WAF scheme are illustrated in Fig. 3. In the following each of these steps is outlined in more detail.

2.2.1. Step 1: solution of the Riemann problem

Various approaches for extending the WAF method to three-dimensional structured grids are discussed in [162]. Applications of the WAF scheme to unstructured grids in two space dimensions are presented to our knowledge only in [164,165]. In the present work we are interested in applying the WAF scheme on three-dimensional unstructured median-dual grids. To this end we adopt the approaches outlined in [166,164,165] which are based on a locally one-dimensional Riemann problem. The Riemann problem at a face between the control volume P_0 and its neighbor $P_{1,f}$ is depicted in Fig. 4. As suggested in [166,164,165] a one-dimensional Riemann problem is obtained for each face by reformulating Eq. (17) in a local coordinate frame $\hat{x}_i$, cf. Fig. 4. The $\hat{x}_1$ axis of this local coordinate frame is aligned with the face normal vector $\vec{n}_f$ [166,164,165], the origin of the local coordinate frame is on the face (i.e. on the intersection between the face and the edge connecting the cell centers of P_0 and $P_{1,f}$, cf. Fig. 4). In this local coordinate frame the vector $\vec{Q}$ is transformed to $\hat{\vec{Q}}=\left(p,\hat{u}_i\right)^T$ where $\hat{u}_i$ denotes the velocity components in the local $\hat{x}_i$ coordinate frame. The initial conditions of the Riemann problem are expressed in terms of a left state $\hat{\vec{Q}}_L$ and a right state $\hat{\vec{Q}}_R$ (cf. Fig. 4) as

$$\hat{\vec{Q}}\left(\hat{x}_1,t=0\right)=\begin{cases}\hat{\vec{Q}}_L=\hat{\vec{Q}}_{P_0}^{\star}\,, & \hat{x}_1<0\\ \hat{\vec{Q}}_R=\hat{\vec{Q}}_{P_{1,f}}^{\star}\,, & \hat{x}_1\geq 0\end{cases}. \tag{19}$$

Pressure and $\hat{u}_1$-velocity evolve in this one-dimensional Riemann problem according to

$$\frac{\partial}{\partial t}\begin{pmatrix}p\\ \hat{u}_1\end{pmatrix}+\begin{pmatrix}0 & \rho c^2\\ \rho^{-1} & 0\end{pmatrix}\frac{\partial}{\partial\hat{x}_1}\begin{pmatrix}p\\ \hat{u}_1\end{pmatrix}=\begin{pmatrix}0\\ 0\end{pmatrix}. \tag{20}$$

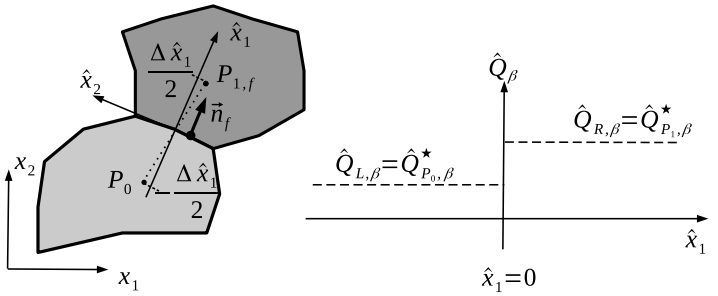

Fig. 4. Quasi one-dimensional Riemann problem at the cell face f between control volumes P_0 and $P_{1,f}$ in the local $\hat{x}_1$-$\hat{x}_2$ coordinate frame. $\hat{Q}_\beta$ denotes the β component of the vector $\hat{\vec{Q}}$.

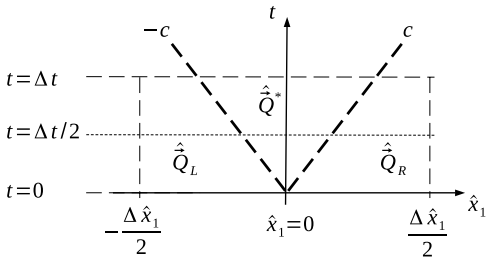

Fig. 5. Solution structure of the Riemann problem in the $\hat{x}_1$-t plane.

All other quantities (i.e. the tangential velocities $\hat{u}_2$ and $\hat{u}_3$, the specific entropy and species mass fractions) remain constant over time. The Eigenvalues of the coefficient matrix of Eq. (20) (i.e. the characteristic speeds) are $\lambda_1 = -c$ and $\lambda_2 = c$. Since there are no Rankine-Hugoniot relations available for Eq. (20) to determine the speed of waves we assume that the wave speeds are equal to these characteristic speeds. Thus, the following derivation is limited to flows with pressure waves of comparatively small amplitude (the method is however applicable to nonlinear problems as demonstrated in Sec. 3.6). On the basis of this assumption the solution of the Riemann problem is advanced in time. The structure of the solution in the $\hat{x}_1$-t plane is shown in Fig. 5. Between the "left" state $\bullet_L$ and the "right" state $\bullet_R$ lies the "star region" $\bullet^*$ which is enclosed by the characteristics of the Eigenvalues $-c$ and c. In the WAF scheme we require the solution of the Riemann problem at the time $\Delta t/2$ which we denote as $\hat{\vec{Q}}(\hat{x}_1, \Delta t/2)$. Thus, a solution for the unknown state $\hat{\vec{Q}}^*$ inside the star region is required. To this end we follow the approach outlined in [167] and consider characteristic equations along the left and right running characteristics (i.e. for the Eigenvalues $-c$ and c). For the left running characteristic (i.e. for $\lambda_1 = -c$) we obtain

$$\frac{1}{c}\left(\frac{\partial p}{\partial t} - \rho c \frac{\partial \hat{u}_1}{\partial t}\right) - \left(\frac{\partial p}{\partial \hat{x}_1} - \rho c \frac{\partial \hat{u}_1}{\partial \hat{x}_1}\right) = 0 \tag{21}$$

whereas we have

$$\frac{1}{c}\left(\frac{\partial p}{\partial t} + \rho c \frac{\partial \hat{u}_1}{\partial t}\right) + \frac{\partial p}{\partial \hat{x}_1} + \rho c \frac{\partial \hat{u}_1}{\partial \hat{x}_1} = 0 \tag{22}$$

for the right running characteristic (i.e. for $\lambda_2 = c$). As in [167] we take the product ρc and c to be constant along the characteristic

$$\rho c \approx \overline{\rho c} = \frac{1}{4}\left(\rho_L + \rho_R\right)\left(c_L + c_R\right) = \frac{1}{4}\left(\rho^\star_{P_0} + \rho^\star_{P_{1,f}}\right)\left(c^\star_{P_0} + c^\star_{P_{1,f}}\right) \tag{23}$$

$$c \approx \overline{c} = \frac{1}{2}(c_L + c_R) = \frac{1}{2}(c^\star_{P_0} + c^\star_{P_{1,f}}) \tag{24}$$

and obtain

$$\frac{\partial}{\partial t}\left(p - \overline{\rho c}\,\hat{u}_1\right) + (-\overline{c})\frac{\partial}{\partial \hat{x}_1}\left(p - \overline{\rho c}\,\hat{u}_1\right) = 0 \tag{25}$$

$$\frac{\partial}{\partial t}\left(p + \overline{\rho c}\,\hat{u}_1\right) + \overline{c}\frac{\partial}{\partial \hat{x}_1}\left(p + \overline{\rho c}\,\hat{u}_1\right) = 0 \tag{26}$$

for the left and right running characteristics, respectively. This yields

$$p - \overline{\rho c}\,\hat{u}_1 = const. \tag{27}$$

$$p + \overline{\rho c}\,\hat{u}_1 = const. \tag{28}$$

or

$$p_L - \overline{\rho c}\,\hat{u}_{1,L} = p^* - \overline{\rho c}\,\hat{u}_1^* \tag{29}$$

$$p_R + \overline{\rho c}\,\hat{u}_{1,R} = p^* + \overline{\rho c}\,\hat{u}_1^* \quad . \tag{30}$$

Solving for pressure and velocity in the star region gives

$$p^* = \frac{p_L + p_R}{2} + \overline{\rho c}\,\frac{\hat{u}_{1,L} - \hat{u}_{1,R}}{2} = \frac{p^\star_{P_0} + p^\star_{P_{1,f}}}{2} + \overline{\rho c}\,\frac{\hat{u}^\star_{1,P_0} - \hat{u}^\star_{1,P_{1,f}}}{2} \tag{31}$$

$$\hat{u}_1^* = \frac{\hat{u}_{1,L} + \hat{u}_{1,R}}{2} + \frac{1}{\overline{\rho c}}\,\frac{p_L - p_R}{2} = \frac{\hat{u}^\star_{1,P_0} + \hat{u}^\star_{1,P_{1,f}}}{2} + \frac{1}{\overline{\rho c}}\,\frac{p^\star_{P_0} - p^\star_{P_{1,f}}}{2} \quad . \tag{32}$$

Using the solution in the star region the complete solution of the Riemann problem reads:

$$\hat{\tilde{Q}}(\hat{x}_1, \Delta t/2) = \begin{cases} \begin{pmatrix} p_L \\ \hat{u}_{i,L} \end{pmatrix} = \begin{pmatrix} p^\star_{P_0} \\ \hat{u}^\star_{i,P_0} \end{pmatrix}, \ \hat{x}_1 \le -\frac{\overline{c}\Delta t}{2} \\ \begin{pmatrix} \frac{p_L+p_R}{2} + \overline{\rho c}\,\frac{\hat{u}_{1,L}-\hat{u}_{1,R}}{2} \\ \frac{\hat{u}_{1,L}+\hat{u}_{1,R}}{2} + \frac{1}{\overline{\rho c}}\,\frac{p_L-p_R}{2} \\ \hat{u}_{2,L} \\ \hat{u}_{3,L} \end{pmatrix} = \begin{pmatrix} \frac{p^\star_{P_0}+p^\star_{P_{1,f}}}{2} + \overline{\rho c}\,\frac{\hat{u}^\star_{1,P_0}-\hat{u}^\star_{1,P_{1,f}}}{2} \\ \frac{\hat{u}^\star_{1,P_0}+\hat{u}^\star_{1,P_{1,f}}}{2} + \frac{1}{\overline{\rho c}}\,\frac{p^\star_{P_0}-p^\star_{P_{1,f}}}{2} \\ \hat{u}^\star_{2,P_0} \\ \hat{u}^\star_{3,P_0} \end{pmatrix}, \ -\frac{\overline{c}\Delta t}{2} < \hat{x}_1 \le 0 \\ \begin{pmatrix} \frac{p_L+p_R}{2} + \overline{\rho c}\,\frac{\hat{u}_{1,L}-\hat{u}_{1,R}}{2} \\ \frac{\hat{u}_{1,L}+\hat{u}_{1,R}}{2} + \frac{1}{\overline{\rho c}}\,\frac{p_L-p_R}{2} \\ \hat{u}_{2,R} \\ \hat{u}_{3,R} \end{pmatrix} = \begin{pmatrix} \frac{p^\star_{P_0}+p^\star_{P_{1,f}}}{2} + \overline{\rho c}\,\frac{\hat{u}^\star_{1,P_0}-\hat{u}^\star_{1,P_{1,f}}}{2} \\ \frac{\hat{u}^\star_{1,P_0}+\hat{u}^\star_{1,P_{1,f}}}{2} + \frac{1}{\overline{\rho c}}\,\frac{p^\star_{P_0}-p^\star_{P_{1,f}}}{2} \\ \hat{u}^\star_{2,P_{1,f}} \\ \hat{u}^\star_{3,P_{1,f}} \end{pmatrix}, \ 0 < \hat{x}_1 \le \frac{\overline{c}\Delta t}{2} \\ \begin{pmatrix} p_R \\ \hat{u}_{i,R} \end{pmatrix} = \begin{pmatrix} p^\star_{P_{1,f}} \\ \hat{u}^\star_{i,P_{1,f}} \end{pmatrix}, \ \frac{\overline{c}\Delta t}{2} < \hat{x}_1 \end{cases} \tag{33}$$

Specific entropy and composition in terms of species mass fractions remain constant over time, i.e.

$$\begin{pmatrix} s(\hat{x}_1, \Delta t/2) \\ Y_\alpha(\hat{x}_1, \Delta t/2) \end{pmatrix} = \begin{cases} \begin{pmatrix} s_L \\ Y_{\alpha,L} \end{pmatrix} = \begin{pmatrix} s^\star_{P_0} \\ Y^\star_{\alpha,P_0} \end{pmatrix}, \ \hat{x}_1 \le 0 \\ \begin{pmatrix} s_R \\ Y_{\alpha,R} \end{pmatrix} = \begin{pmatrix} s^\star_{P_{1,f}} \\ Y^\star_{\alpha,P_{1,f}} \end{pmatrix}, \ 0 < \hat{x}_1 \end{cases} \quad . \tag{34}$$

In addition, the density and the square speed of sound are required in this Riemann problem in order to evaluate the coefficient matrices. We first compute the values of density (i.e. ρ^{*L} and ρ^{*R}) and the square speed of sound (i.e. $c^{2,*L}$ and $c^{2,*R}$) in the "star region", i.e.

$$\rho^{*L} = \rho\left(p^*, s^\star_{P_0}, Y^\star_{\alpha,P_0}\right) \tag{35}$$

$$\rho^{*R} = \rho\left(p^*, s^\star_{P_{1,f}}, Y^\star_{\alpha,P_{1,f}}\right) \tag{36}$$

$$c^{2,*L} = c^2\left(p^*, s^\star_{P_0}, Y^\star_{\alpha,P_0}\right) \tag{37}$$

$$c^{2,*R} = c^2\left(p^*, s^\star_{P_{1,f}}, Y^\star_{\alpha,P_{1,f}}\right) \tag{38}$$

where p^* is given by Eq. (31). Note that there are two different values for density and speed of sound in the "star region" since specific entropy and mass fractions may change at $\hat{x}_1 = 0$ as Eq. (34) indicates. The situation is depicted in Fig. 6 where a "left star region" $\bullet^{*L}$ and a "right star region" $\bullet^{*R}$ are shown for density and square speed of sound. The solution for density and square speed of sound in this Riemann problem is given at the time $\Delta t/2$ by

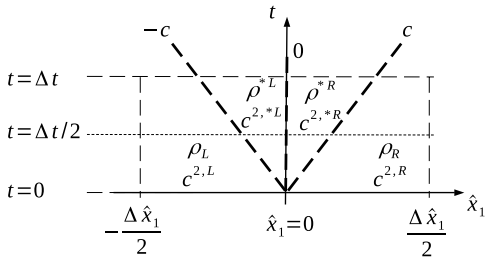

Fig. 6. Solution structure of the Riemann problem in the $\hat{x}_1$-t plane with regions for the density and the square speed of sound.

$$\begin{pmatrix} \rho(\hat{x}_1, \Delta t/2) \\ c^2(\hat{x}_1, \Delta t/2) \end{pmatrix} = \begin{cases} \begin{pmatrix} \rho_L \\ c_L^2 \end{pmatrix} = \begin{pmatrix} \rho_{P_0}^\star \\ c_{P_0}^{2\star} \end{pmatrix}, \ \hat{x}_1 \leq -\frac{\overline{c}\Delta t}{2} \\ \begin{pmatrix} \rho^{*L} \\ c^{2,*L} \end{pmatrix} = \begin{pmatrix} \rho\left(p^*, s_{P_0}^\star, Y_{\alpha,P_0}^\star\right) \\ c^2\left(p^*, s_{P_0}^\star, Y_{\alpha,P_0}^\star\right) \end{pmatrix}, \ -\frac{\overline{c}\Delta t}{2} < \hat{x}_1 \leq 0 \\ \begin{pmatrix} \rho^{*R} \\ c^{2,*R} \end{pmatrix} = \begin{pmatrix} \rho\left(p^*, s_{P_{1,f}}^\star, Y_{\alpha,P_{1,f}}^\star\right) \\ c^2\left(p^*, s_{P_{1,f}}^\star, Y_{\alpha,P_{1,f}}^\star\right) \end{pmatrix}, \ 0 < \hat{x}_1 \leq \frac{\overline{c}\Delta t}{2} \\ \begin{pmatrix} \rho_R \\ c_R^2 \end{pmatrix} = \begin{pmatrix} \rho_{P_{1,f}}^\star \\ c_{P_{1,f}}^{2\star} \end{pmatrix}, \ \frac{\overline{c}\Delta t}{2} < \hat{x}_1 \end{cases} . \tag{39}$$

2.2.2. Step 2: computation of face values

In the WAF method the face value $\vec{Q}_f^{\star+\frac{1}{2}}$ in Eq. (18) is defined at $\Delta t/2$ (or time level $\star + \frac{1}{2}$) as the spatial average of the solution to the Riemann problem defined by Eqs. (19) and (20) [162]. This average is evaluated in the local coordinate frame first, i.e.

$$\hat{\vec{Q}}_f^{\star+\frac{1}{2}} = \frac{1}{\Delta\hat{x}_1} \int_{-\Delta\hat{x}_1/2}^{\Delta\hat{x}_1/2} \hat{\vec{Q}}(\hat{x}_1, \Delta t/2)\, d\hat{x}_1 \ , \tag{40}$$

where $\Delta\hat{x}_1$ is the distance between the centers of the control volumes in $\hat{x}_1$ direction as illustrated in Fig. 4. By transforming in a last step $\hat{\vec{Q}}_f^{\star+\frac{1}{2}}$ into the global coordinate frame the face value $\vec{Q}_f^{\star+\frac{1}{2}}$ is obtained. Hence, applying Eq. (33) in Eq. (40) and transforming the velocity from the local coordinate frame to the global coordinate frame provides the required pressure $p_f^{\star+\frac{1}{2}}$ and velocity $\vec{u}_f^{\star+\frac{1}{2}}$ at the face f, i.e.

$$\begin{aligned} p_f^{\star+\frac{1}{2}} &= \frac{p_L + p_R}{2} + \nu_f\, \overline{\rho c}\, \frac{\langle \vec{u}_L - \vec{u}_R, \vec{e}_f \rangle}{2} \\ &= \frac{p_{P_0}^\star + p_{P_{1,f}}^\star}{2} + \nu_f\, \overline{\rho c}\, \frac{\langle \vec{u}_{P_0}^\star - \vec{u}_{P_{1,f}^\star}, \vec{e}_f \rangle}{2} \end{aligned} \tag{41}$$

$$\begin{aligned} \vec{u}_f^{\star+\frac{1}{2}} &= \frac{\vec{u}_L + \vec{u}_R}{2} + \frac{\nu_f}{\overline{\rho c}}\, \frac{p_L - p_R}{2}\, \vec{e}_f \\ &= \frac{\vec{u}_{P_0}^\star + \vec{u}_{P_{1,f}}^\star}{2} + \frac{\nu_f}{\overline{\rho c}}\, \frac{p_{P_0}^\star - p_{P_{1,f}}^\star}{2}\, \vec{e}_f \end{aligned} \tag{42}$$

where the operator $\langle \vec{\bullet}, \vec{\bullet} \rangle$ denotes the scalar product of two vectors and $\vec{e}_f = \vec{n}_f / \|\vec{n}_f\|$ the unit vector in direction of the face normal. The acoustic Courant-Friedrichs-Lewis (CFL) number ν_f at the face f is defined as

$$\nu_f = \frac{\overline{c}\ \Delta t}{\Delta\hat{x}_1} \ . \tag{43}$$

The spatial averaging defined by Eq. (40) is also required for the computation of $\langle \rho \rangle_{P_0}$ and $\langle c^2 \rangle_{P_0}$ in the averaged coefficient matrices of Eq. (18). We use Eq. (39) in Eq. (40) in order to obtain first for each individual face the values

$$\rho_f^{\star+\frac{1}{2}} = \nu_f \frac{\rho_{P_0}^{\star} + \rho_{P_{1,f}}^{\star}}{2} + (1-\nu_f)\frac{\rho^{*L} + \rho^{*R}}{2} \quad , \tag{44}$$

$$c_f^{2,\star+\frac{1}{2}} = \nu_f \frac{c_{P_0}^{2,\star} + c_{P_{1,f}}^{2,\star}}{2} + (1-\nu_f)\frac{c^{2,*L} + c^{2,*R}}{2} \quad . \tag{45}$$

These face values are used in a following step to compute the averaged coefficient matrices.

2.2.3. Step 3: computation of averaged coefficient matrices

With the help Eqs. (44) and (45) the face averages $\langle\rho\rangle_{P_0}$ and $\langle c^2\rangle_{P_0}$ are defined as [162]

$$\langle\rho\rangle_{P_0} = \frac{1}{N_{F,P_0}} \sum_{f=1}^{N_{F,P_0}} \rho_f^{\star+\frac{1}{2}} \quad , \tag{46}$$

$$\langle c^2\rangle_{P_0} = \frac{1}{N_{F,P_0}} \sum_{f=1}^{N_{F,P_0}} c_f^{2,\star+\frac{1}{2}} \quad . \tag{47}$$

These values are used to compute the averaged coefficient matrices in Eq. (18).

2.2.4. Step 4: formulation of explicit WAF scheme

We substitute the results given by Eqs. (41) and (42) in Eq. (18). Hence, an explicit WAF scheme, which advances the solution in a control volume P_0 during the acoustic step, is given by

$$\Delta V_{P_0} \frac{p_{P_0}^{n+1} - p_{P_0}^{\star}}{\Delta t} = -\langle\rho\rangle_{P_0}\langle c^2\rangle_{P_0} \sum_{f=1}^{N_{F,P_0}} \frac{\langle \vec{u}_{P_0}^{\star} + \vec{u}_{P_{1,f}}^{\star}, \vec{n}_f\rangle}{2} + \|\vec{n}_f\| \frac{\nu_f}{\overline{\rho c}_f} \frac{p_{P_0}^{\star} - p_{P_{1,f}}^{\star}}{2} \quad , \tag{48}$$

$$\Delta V_{P_0} \frac{u_{i,P_0}^{n+1} - u_{i,P_0}^{\star}}{\Delta t} = -\frac{1}{\langle\rho\rangle_{P_0}} \sum_{f=1}^{N_{F,P_0}} n_{f,i} \left(\frac{p_{P_0}^{\star} + p_{P_{1,f}}^{\star}}{2} + \nu_f \, \overline{\rho c}_f \frac{\langle \vec{u}_{P_0}^{\star} - \vec{u}_{P_{1,f}}^{\star}, \vec{e}_f\rangle}{2} \right) \quad . \tag{49}$$

From Eqs. (15) and (16) we have

$$s_{P_0}^{n+1} = s_{P_0}^{\star} \quad , \tag{50}$$

and

$$Y_{\alpha,P_0}^{n+1} = Y_{\alpha,P_0}^{\star} \quad . \tag{51}$$

2.3. Implicit formulation of the WAF scheme

A quite restrictive drawback of the explicit scheme presented in the previous section (cf. Eqs. (48) and (49)) is that it requires $\nu_f \leq 1$ to remain stable. In the following an implicit formulation is given overcoming this limitation. As noted in [162] the WAF scheme is equivalent to the second order Lax-Wendroff scheme [168]. Thus, we use the approach of Lerat [169–171] to derive an implicit WAF scheme for the acoustic step. We obtain the equations

$$\Delta V_{P_0} \frac{\Delta p_{P_0}}{\Delta t} + \langle\rho\rangle_{P_0}\langle c^2\rangle_{P_0} \sum_{f=1}^{N_{F,P_0}} \|\vec{n}_f\| \frac{\nu_f}{\overline{\rho c}_f} \frac{\Delta p_{P_0} - \Delta p_{P_{1,f}}}{4} = -\langle\rho\rangle_{P_0}\langle c^2\rangle_{P_0} \sum_{f=1}^{N_{F,P_0}} \frac{\langle \vec{u}_{P_0}^{\star} + \vec{u}_{P_{1,f}}^{\star}, \vec{n}_f\rangle}{2} + \|\vec{n}_f\| \frac{\nu_f}{\overline{\rho c}_f} \frac{p_{P_0}^{\star} - p_{P_{1,f}}^{\star}}{2} \tag{52}$$

and

$$\Delta V_{P_0} \frac{\Delta u_{i,P_0}}{\Delta t} - \frac{\gamma}{\langle\rho\rangle_{P_0}} \sum_{f=1}^{N_{F,P_0}} n_{f,i} \frac{\overline{\rho c}_f}{\nu_f} \frac{\langle \Delta\vec{u}_{P_0} - \Delta\vec{u}_{P_{1,f}}, \vec{e}_f\rangle}{2} = -\frac{1}{\langle\rho\rangle_{P_0}} \sum_{f=1}^{N_{F,P_0}} n_{f,i} \frac{p_{P_0}^{\star} + p_{P_{1,f}}^{\star} + p_{P_0}^{n+1} + p_{P_{1,f}}^{n+1}}{4} \quad , \tag{53}$$

where the unknowns are denoted by $\Delta u_{i,P_0} = u_{i,P_0}^{n+1} - u_{i,P_0}^{\star}$ and $\Delta p_{P_0} = p_{P_0}^{n+1} - p_{P_0}^{\star}$. Here, different time discretizations are used for velocity and pressure which permits a sequential solution of these two equations. First the pressure equation given by Eq. (52) is solved. Subsequently, the velocity equation given by Eq. (53) is solved using the newly obtained pressure. The parameter γ is used to control the implicit scheme for the velocity equation, where second order accuracy requires $\gamma < 1/2$ [171]. The matrices of the linear systems given by Eqs. (52) and (53) are not symmetric for unstructured meshes. Even for an equidistant structured mesh the matrices are not symmetric since ν_f and $\overline{\rho c}_f$ (which are required to compute the matrix coefficients at a point P_0) vary on the faces of a control volume at P_0. Symmetric matrices are only obtained for model problems such as in Sec. 2.4. It can be shown, however, that the matrix of the linear system given by Eq. (52) is positive definite by applying Gershgorin's circle theorem [172] to its symmetric

part [173]. In the same way we can show that the matrix of the linear system given by Eq. (53) is also positive definite except for certain ranges of the parameter γ. To solve the linear systems (52) and (53), Krylov space solvers are used in ThetaCOM. In this work we use the Bi-Conjugate Gradient Stabilized (BiCGSTAB) method [174] in conjunction with a Jacobi preconditioner (i.e. the linear system is scaled with the inverse of the linear system's diagonal). The stability of the implicit approach is discussed in the following section.

2.4. Stability

To investigate the stability of the WAF scheme we apply the von Neumann stability analysis to the following linear, hyperbolic model problem

$$\frac{\partial U}{\partial t} + c_c \frac{\partial U}{\partial x_1} + c_a \frac{\partial V}{\partial x_1} = 0 \tag{54}$$

$$\frac{\partial V}{\partial t} + c_c \frac{\partial V}{\partial x_1} + c_a \frac{\partial U}{\partial x_1} = 0 \ , \tag{55}$$

where U and V are the transported variables and c_c and c_a mimic the convective and acoustic wave speeds, respectively. The Eigenvalues of this system are $c_c + c_a$ and $c_c - c_a$. Applying the ICS scheme yields the advective step

$$\frac{\partial U}{\partial t} + c_c \frac{\partial U}{\partial x_1} = 0 \tag{56}$$

$$\frac{\partial V}{\partial t} + c_c \frac{\partial V}{\partial x_1} = 0 \tag{57}$$

and the acoustic step

$$\frac{\partial U}{\partial t} + c_a \frac{\partial V}{\partial x_1} = 0 \tag{58}$$

$$\frac{\partial V}{\partial t} + c_a \frac{\partial U}{\partial x_1} = 0 \ . \tag{59}$$

To solve Eqs. (56) and (57) numerically we use time and space centered scheme as in [32] which yields

$$\left[1 + \frac{\nu_c}{4}\,\bar{\delta}\right] U_l^{\star} = \left[1 - \frac{\nu_c}{4}\,\bar{\delta}\right] U_l^{n} \tag{60}$$

$$\left[1 + \frac{\nu_c}{4}\,\bar{\delta}\right] V_l^{\star} = \left[1 - \frac{\nu_c}{4}\,\bar{\delta}\right] V_l^{n} \tag{61}$$

whereas for Eqs. (58) and (59) we employ the implicit WAF scheme given in Sec. 2.3 leading to

$$\left[1 - \frac{\nu_a^2}{4}\,\delta^2\right] U_l^{n+1} = \left[-\frac{\nu_a}{2}\,\bar{\delta}\right] V_l^{\star} + \left[1 + \frac{\nu_a^2}{4}\,\delta^2\right] U_l^{\star} \tag{62}$$

$$\left[1 + \frac{\gamma}{2}\,\delta^2\right] V_l^{n+1} + \left[\frac{\nu_a}{4}\,\bar{\delta}\right] U_l^{n+1} = \left[-\frac{\nu_a}{4}\,\bar{\delta}\right] U_l^{\star} + \left[1 + \frac{\gamma}{2}\,\delta^2\right] V_l^{\star} \ . \tag{63}$$

The operators δ^2 and $\bar{\delta}$ are defined as in [175] to

$$\bar{\delta} U_l = U_{l+1} - U_{l-1}$$

$$\delta^2 U_l = U_{l+1} + U_{l-1} - 2\,U_l$$

and the CFL numbers ν_c and ν_a are given by

$$\nu_c = \frac{c_c\,\Delta t}{\Delta x_1} \ , \quad \nu_a = \frac{c_a\,\Delta t}{\Delta x_1} \ .$$

The one dimensional computational domain is of finite length and is taken to be divided into M computational cells with a width of Δx_1. We assume periodic boundary conditions and express $U_l^{\bullet}$ and $V_l^{\bullet}$ in space by the finite Fourier series [175]

$$U_l^{\bullet} = \sum_{m=-M}^{M} \xi_m^{\bullet}\, e^{l k_m \Delta x_1 \mathrm{i}}$$

$$V_l^{\bullet} = \sum_{m=-M}^{M} \eta_m^{\bullet}\, e^{l k_m \Delta x_1 \mathrm{i}}$$

where the symbol $\bullet$ represents either the time level n, $\star$ or $n+1$. $\mathrm{i} = \sqrt{-1}$ is the imaginary unit and k_m is the wave number of the mth harmonic. $\xi_m^{\bullet}$ and $\eta_m^{\bullet}$ represent the amplitudes of the mth harmonic. Using these Fourier expansions in the advective step (Eqs. (60) and (61)) and the acoustic step (Eqs. (62) and (63)) we obtain for a single harmonic m of the Fourier series

$$\begin{pmatrix} \xi_m^\star \\ \eta_m^\star \end{pmatrix} = \underline{\underline{G}}_{c,m} \begin{pmatrix} \xi_m^n \\ \eta_m^n \end{pmatrix} \tag{64}$$

$$\begin{pmatrix} \xi_m^{n+1} \\ \eta_m^{n+1} \end{pmatrix} = \underline{\underline{G}}_{a,m} \begin{pmatrix} \xi_m^\star \\ \eta_m^\star \end{pmatrix} \tag{65}$$

where the amplification matrices $\underline{\underline{G}}_{c,m}$ and $\underline{\underline{G}}_{a,m}$ are given by

$$\underline{\underline{G}}_{c,m} = e^{2\theta_m \mathrm{i}} \begin{pmatrix} 1 & 0 \\ 0 & 1 \end{pmatrix} \ , \tag{66}$$

$$\underline{\underline{G}}_{a,m} = \frac{1}{1 - \frac{\nu_a^2}{2}(\cos\beta_m - 1)} \begin{pmatrix} 1 + \frac{\nu_a^2}{2}(\cos\beta_m - 1) & -\nu_a \sin\beta_m \mathrm{i} \\ \frac{-\nu_a \sin\beta_m \mathrm{i}}{1+\gamma(\cos\beta_m - 1)} & \frac{(1+\gamma(\cos\beta_m-1))\ (1-\frac{\nu_a^2}{2}(\cos\beta_m-1)) - \frac{\nu_a^2 \sin^2\beta_m}{2}}{1+\gamma(\cos\beta_m-1)} \end{pmatrix} \tag{67}$$

and β_m and θ_m are defined as

$$\beta_m = k_m \Delta x_1 = \frac{m\,\pi}{M} \ ,$$
$$\theta_m = -\arctan\left(2\nu_c \sin\beta_m\right) \ .$$

To obtain the amplification matrix for one harmonic over the entire time step Eqs. (64) and (65) are combined as suggested in [37] to

$$\begin{pmatrix} \xi_m^{n+1} \\ \eta_m^{n+1} \end{pmatrix} = \underline{\underline{G}}_m \begin{pmatrix} \xi_m^n \\ \eta_m^n \end{pmatrix} \tag{68}$$

where

$$\underline{\underline{G}}_m = \underline{\underline{G}}_{a,m}\, \underline{\underline{G}}_{c,m} = e^{2\theta_m \mathrm{i}}\, \underline{\underline{G}}_{a,m} \tag{69}$$

is the overall amplification matrix. For stability we demand that none of the individual harmonics is amplified [176]. A necessary condition for stability is the von Neumann condition [176]

$$|\lambda_q^{G_m}| \leq 1 + O(\Delta t) \tag{70}$$

where $\lambda_q^{G_m}$ denotes the q-th Eigenvalue of $\underline{\underline{G}}_m$. This inequality must be fulfilled for every Eigenvalue at all wave numbers k_m, any time step size Δt and time $t = n\Delta t$ of the computation's nth time step [176]. For $\underline{\underline{G}}_{a,m}$ and $\underline{\underline{G}}_m$ we have the following lemma:

Lemma 1. *The amplification matrices $\underline{\underline{G}}_{a,m}$ and $\underline{\underline{G}}_m$ fulfill the von Neumann necessary condition.*

Proof. We first define the auxiliary functions

$$a_\lambda(\nu_a, \beta_m) = \frac{\nu_a^2}{2}(\cos\beta_m - 1)$$
$$b_\lambda(\nu_a, \beta_m) = \frac{\nu_a}{2}\sin\beta_m$$
$$g_\lambda(\gamma, \beta_m) = 1 + \gamma\ (\cos\beta_m - 1)$$

and express the matrix $\underline{\underline{G}}_{a,m}$ as

$$\underline{\underline{G}}_{a,m} = \frac{1}{1 - a_\lambda} \begin{pmatrix} 1 + a_\lambda & -2b_\lambda \mathrm{i} \\ \frac{-2b_\lambda \mathrm{i}}{g_\lambda} & \frac{g_\lambda\ (1-a_\lambda) - 2b_\lambda^2}{g_\lambda} \end{pmatrix} \ .$$

The two Eigenvalues of $\underline{\underline{G}}_{a,m}$ are given by

$$\lambda_{1,2}^{G_{a,m}} = \frac{1}{g_\lambda(1 - a_\lambda)} \left(-B_\lambda \pm \sqrt{B_\lambda^2 - C_\lambda} \right) \tag{71}$$

which are either real or complex depending on the sign of $B_\lambda^2 - C_\lambda$ where B_λ and C_λ are given by

$$B_\lambda = b_\lambda^2 - g_\lambda$$
$$C_\lambda = g_\lambda(1-a_\lambda)(g_\lambda(1+a_\lambda)+2\ b_\lambda^2)\ .$$

In order to prove Lemma 1 we show first for $\underline{\underline{G}}_{a,m}$ that

$$\rho_{G_{a,m}} := \max\left(|\lambda_1^{G_{a,m}}|, |\lambda_2^{G_{a,m}}|\right) \leq 1 \tag{72}$$

is fulfilled, where $\rho_{G_{a,m}}$ denotes the spectral radius of $\underline{\underline{G}}_{a,m}$. We consider first real Eigenvalues (i.e. $B_\lambda^2 - C_\lambda \geq 0$) where Eq. (72) yields

$$\begin{aligned}
&\rho_{G_{a,m}} \leq 1 \\
\Rightarrow\ &\frac{|B_\lambda| + \sqrt{B_\lambda^2 - C_\lambda}}{g_\lambda(1-a_\lambda)} \leq 1 \\
\Rightarrow\ &0 \leq g_\lambda\ \vee\ 0 \leq b_\lambda^2
\end{aligned}$$

which is always true for $\gamma < 1/2$, i.e. for second order schemes, and any choice of β_m and ν_a. If we apply Eq. (72) to complex Eigenvalues (i.e. $B_\lambda^2 - C_\lambda < 0$) we obtain a similar result in terms of γ, i.e.

$$\begin{aligned}
&\rho_{G_{a,m}} \leq 1 \\
\Rightarrow\ &\frac{\sqrt{C_\lambda}}{g_\lambda(1-a_\lambda)} \leq 1 \\
\Rightarrow\ &\gamma \leq \frac{1}{2}\ .
\end{aligned}$$

Thus $\underline{\underline{G}}_{a,m}$ fulfills the von Neumann necessary condition. Due to Eq. (69) we have

$$\begin{aligned}
&\lambda_q^{G_m} = e^{2\theta_m \mathrm{i}}\lambda_q^{G_{a,m}} \\
\Rightarrow\ &|\lambda_q^{G_m}| = |\lambda_q^{G_{a,m}}|
\end{aligned}$$

and therefore

$$\rho_{G_m} = \rho_{G_{a,m}} \tag{73}$$
$$\Rightarrow \rho_{G_m} \leq 1 \tag{74}$$

where ρ_{G_m} is the spectral radius of $\underline{\underline{G}}_m$. Hence, both $\underline{\underline{G}}_{a,m}$ and $\underline{\underline{G}}_m$ fulfill the von Neumann necessary condition. □

Lemma 1 represents a necessary condition for stability. To obtain sufficient conditions we first consider the Fourier modes $m \in \{-M, 0, M\}$, i.e. $\beta_m \in \{-\pi; 0; \pi\}$, where the following lemma applies.

Lemma 2. *For $\beta_m \in \{-\pi; 0; \pi\}$ the matrices $\underline{\underline{G}}_{a,m}$ and $\underline{\underline{G}}_m$ are stable.*

Proof. The von Neumann necessary condition is also a sufficient condition if the amplification matrices $\underline{\underline{G}}_{a,m}$ and $\underline{\underline{G}}_m$ are normal matrices [176]. Such a situation occurs if $\beta_m \in \{-\pi; 0; \pi\}$ because in this $\underline{\underline{G}}_{a,m}$ and $\underline{\underline{G}}_m$ become a real valued diagonal matrices which is the trivial case of a normal matrix. □

For any other value of β_m a sufficient condition of stability is obtained here through the use of the Kreiss Matrix Theorem [176]. In order to use the Kreiss Matrix Theorem in this work the following lemma is required.

Lemma 3. *The spectral radius of the matrix $\underline{\underline{G}}_{a,m}$ (and subsequently of the matrix $\underline{\underline{G}}_m$) equals one only for $\beta_m \in \{-\pi; 0; \pi\}$ provided that a second order scheme is used (i.e. $\gamma < 1/2$).*

Proof. To prove Lemma 3 we simply solve the equation

$$\rho_{G_{a,m}} = 1\ .$$

For real Eigenvalues we obtain

$$\rho_{G_{a,m}} = 1$$
$$\Rightarrow \sin\beta_m = 0 \quad \vee \quad \left(\gamma = \frac{1}{2} \wedge \cos\beta_m = -1\right)$$

From these two conditions only $\sin\beta_m = 0$, i.e. $\beta_m \in \{-\pi; 0; \pi\}$ is considered here since we require $\gamma < 1/2$. For complex Eigenvalues we get

$$\rho_{G_{a,m}} = 1$$
$$\Rightarrow \cos\beta_m = 1 \quad \vee \quad \gamma = \frac{1}{2} \quad .$$

Again, only the first condition $\cos\beta_m = 1$, i.e. $\beta_m = 0$, is retained. Hence, the spectral radius equals one only for $\beta_m \in \{-\pi; 0; \pi\}$. Due to Eq. (73) this result also applies to the matrix $\underline{\underline{G}}_m$. □

To continue the proof of stability on the basis of the Kreiss Matrix Theorem we consider a family $\mathscr{F}$ of $q \times q$ matrices $\underline{\underline{A}}_{\mathscr{F}}$ [176]. This family of matrices is said to be stable if there exists a constant $\mathscr{C}$ such that for all $\underline{\underline{A}}_{\mathscr{F}} \in \mathscr{F}$ and all positive integers k [176]

$$\|\underline{\underline{A}}_{\mathscr{F}}\|^k < \mathscr{C} \quad . \tag{75}$$

We use the following statement of the Kreiss Matrix Theorem to prove stability [176]:

Theorem 1. *The stability of the family $\mathscr{F}$ of matrices $\underline{\underline{A}}_{\mathscr{F}}$ is equivalent to the following statement:*
There exist constants $\mathscr{C}_S$ and $\mathscr{C}_B$ and, to each $\underline{\underline{A}}_{\mathscr{F}} \in \mathscr{F}$, a non-singular matrix $\underline{\underline{S}}$ such that (i) $\|\underline{\underline{S}}\|$, $\|\underline{\underline{S}}^{-1}\| \leq \mathscr{C}_S$; and (ii) $\underline{\underline{B}}_{\mathscr{F}} = \underline{\underline{S}}\,\underline{\underline{B}}_{\mathscr{F}}\,\underline{\underline{S}}^{-1}$ is upper triangular and its off-diagonal elements satisfy

$$|B_{\mathscr{F},ij}| \leq \mathscr{C}_B \ \min(1 - |\kappa_i|, 1 - |\kappa_j|) \ , \tag{76}$$

where κ_i are the diagonal elements of $\underline{\underline{B}}_{\mathscr{F}}$, i.e., the Eigenvalues of $\underline{\underline{A}}_{\mathscr{F}}$ and $\underline{\underline{B}}_{\mathscr{F}}$.

In this work we choose the family $\mathscr{F} = \left\{\underline{\underline{G}}_{a,m}\right\}$ and impose restrictions on the choice of ν_a and γ. For both ν_a and γ we require that they are bounded, i.e. they do not approach infinity since this case does not represent a meaningful numerical scheme. To obtain a second order numerical scheme we do not consider $\gamma \to 1/2$. Furthermore, we disregard the limit $\nu_a \to 0$ since we have finite values for Δt and Δx_1 as well as a finite wave speed c_a (for compressible flows this speed corresponds to the speed of sound which is nonzero). Hence, we state the following lemma.

Lemma 4. *The amplification matrix $\underline{\underline{G}}_{a,m}$ fulfills the conditions (i) and (ii) of Theorem 1 (Kreiss Matrix Theorem) provided that*

- $\beta_m \in \left[-\frac{(M-1)}{M}\pi; -\frac{\pi}{M}\right] \quad \vee \quad \beta_m \in \left[\frac{\pi}{M}; \frac{(M-1)}{M}\pi\right]$
- *ν_a is bounded and does not approach asymptotically zero.*
- *γ is bounded and does not approach asymptotically one half.*

Proof. We first prove that condition *(i)* is fulfilled. To this end we consider the left Eigenvector $\vec{v}_1$ for the Eigenvalue

$$\lambda_1^{G_{a,m}} = \frac{-B_\lambda + \sqrt{B_\lambda^2 - C_\lambda}}{g_\lambda(1 - a_\lambda)}$$

and the right Eigenvector $\vec{w}_2$ for the Eigenvalue

$$\lambda_2^{G_{a,m}} = \frac{-B_\lambda - \sqrt{B_\lambda^2 - C_\lambda}}{g_\lambda(1 - a_\lambda)} \quad .$$

These Eigenvectors are given by

$$\vec{v}_1 = \frac{1}{\sqrt{4b_\lambda^2 g_\lambda^2 + \left|g_\lambda\left(1 + a_\lambda\right) - \zeta_\lambda\right|^2}} \begin{pmatrix} 2b_\lambda g_\lambda \mathrm{i} \\ g_\lambda(1 + a_\lambda) - \zeta_\lambda \end{pmatrix}$$
$$\vec{w}_2 = \frac{1}{\sqrt{4b_\lambda^2 g_\lambda^2 + \left|g_\lambda\left(1 + a_\lambda\right) - \zeta_\lambda\right|^2}} \begin{pmatrix} -\mathrm{i}\left(g_\lambda(1 + a_\lambda) - \zeta_\lambda\right) \\ -2b_\lambda g_\lambda \end{pmatrix} \quad ,$$

where ζ_λ is given by

$$\zeta_\lambda = g_\lambda - b_\lambda^2 + \sqrt{b_\lambda^4 + g_\lambda^2 a_\lambda^2 + 2 g_\lambda b_\lambda^2 \left(a_\lambda - 2\right)} \in \mathbb{C} \ .$$

$\mathbb{C}$ denotes the set of complex numbers. Using these Eigenvectors the matrix $\underline{\underline{S}}$ and $\underline{\underline{S}}^{-1}$ are defined as

$$\underline{\underline{S}} = \begin{bmatrix} \left(\overline{\vec{v}_1}\right)^T \\ \left(\vec{w}_2\right)^T \end{bmatrix}$$
$$\underline{\underline{S}}^{-1} = \begin{bmatrix} \vec{v}_1, \overline{\vec{w}_2} \end{bmatrix} \ ,$$

where operators $\bar{\bullet}$ and $\bullet^T$ denote the conjugate complex and the transpose, respectively. It can easily be shown that $\underline{\underline{S}}$ is an unitary matrix since the inverse $\underline{\underline{S}}^{-1}$ is also its conjugate transpose. Thus the spectral norm of these matrices is one and we have therefore $\mathscr{C}_S = 1$. Hence condition *(i)* is fulfilled. For the proof of the validity of condition *(ii)* we compute $\underline{\underline{B}}_{\mathscr{F}}$ for the matrix $\underline{\underline{G}}_{a,m}$ and obtain

$$\underline{\underline{B}}_{\mathscr{F}} = \begin{pmatrix} \lambda_1^{G_{a,m}} & \langle \overline{\vec{v}_1}, \underline{\underline{G}}_{a,m} \overline{\vec{w}_2} \rangle \\ 0 & \lambda_2^{G_{a,m}} \end{pmatrix} \ .$$

The upper diagonal matrix consists of a single element $B_{\mathscr{F},12}$ and its magnitude is given by

$$\left|B_{\mathscr{F},12}\right| = \left| \langle \overline{\vec{v}_1}, \underline{\underline{G}}_{a,m} \overline{\vec{w}_2} \rangle \right| = \begin{cases} 2 \frac{\sqrt{(a_\lambda g_\lambda + b_\lambda^2)^2 + b_\lambda^2 (1 - g_\lambda)^2}}{(1 - a_\lambda) g_\lambda}, & B_\lambda^2 - C_\lambda < 0 \\ 2 \frac{|b_\lambda| (g_\lambda + 1)}{(1 - a_\lambda) g_\lambda}, & B_\lambda^2 - C_\lambda \geq 0 \end{cases}$$

Note, that $\left|B_{\mathscr{F},12}\right|$ is a continuous function of its arguments γ, ν and β_m because its denominator is strictly positive in the specified range of the arguments. Since $\left|B_{\mathscr{F},12}\right|$ is finite at the upper and lower limits of the intervals of β_m it is a bounded function and an upper limit of $\left|B_{\mathscr{F},12}\right|$ exists. It remains to show that

$$\begin{aligned} & |B_{\mathscr{F},12}| \leq \mathscr{C}_B \ \min(1 - |\kappa_i|, 1 - |\kappa_j|) \\ \Rightarrow & |B_{\mathscr{F},12}| \leq \mathscr{C}_B \ \left(1 - \rho_{G_{a,m}}\right) \\ \Rightarrow & \frac{|B_{\mathscr{F},12}|}{1 - \rho_{G_{a,m}}} \leq \mathscr{C}_B \ . \end{aligned}$$

For the existence of an upper bound $\mathscr{C}_B$ it is necessary that $|B_{\mathscr{F},12}| / \left(1 - \rho_{G_{a,m}}\right)$ is a bounded function. Due to Lemma 3 we have

$$\begin{aligned} & \rho_{G_{a,m}} < 1, \ \ \beta_m \in \left[-\frac{(M-1)}{M}\pi; -\frac{\pi}{M}\right] \ \vee \ \beta_m \in \left[\frac{\pi}{M}; \frac{(M-1)}{M}\pi\right] \\ \Rightarrow & 1 - \rho_{G_{a,m}} > 0, \ \ \beta_m \in \left[-\frac{(M-1)}{M}\pi; -\frac{\pi}{M}\right] \ \vee \ \beta_m \in \left[\frac{\pi}{M}; \frac{(M-1)}{M}\pi\right] \ . \end{aligned}$$

The function $1/(1 - \rho_{G_{a,m}})$ is therefore a bounded function for the range of β_m considered here (i.e. it is continuous and it also possesses finite values at the upper and lower limits of the β_m intervals). Thus the function $|B_{\mathscr{F},12}| / \left(1 - \rho_{G_{a,m}}\right)$ is also a bounded function which possesses an upper bound. Hence, a constant $\mathscr{C}_B$ exists and condition *(ii)* is fulfilled. □

Lemma 4 establishes that the matrix $\underline{\underline{G}}_{a,m}$ is stable in the sense of Eq. (75). From Eq. (68) we obtain

$$\| \underline{\underline{G}}_m \| = \| e^{2\theta_m \mathrm{i}} \underline{\underline{G}}_{a,m} \| = \| \underline{\underline{G}}_{a,m} \| \ .$$

Hence, according to Eq. (75) the matrix $\underline{\underline{G}}_m$ is also stable in the range of β_m, ν and γ given in Lemma 4. Together with Lemma 2 the stability of $\underline{\underline{G}}_m$ over the entire range of β_m is established.

2.5. Monotonicity

To obtain a monotone scheme a spatially first order scheme is required [177]. To arrive at such a scheme for the acoustic step we make use of Lerat's approach [169–171] to derive a scheme which is first order accurate in space and time. As suggested in [162] a

limiter function ϕ_{P_0} is used to blend the first order scheme and the second order scheme of Sec. 2.3 in order to enforce monotonicity. The monotone scheme for pressure and velocity is then given by

$$\Delta V_{P_0} \frac{\Delta p_{P_0}}{\Delta t} + \langle \rho \rangle_{P_0} \langle c^2 \rangle_{P_0} \sum_{f=1}^{N_{F,P_0}} \|\vec{n}_f\| \, h_{f,LHS,p} \frac{\Delta p_{P_0} - \Delta p_{P_{1,f}}}{2} =$$
$$- \langle \rho \rangle_{P_0} \langle c^2 \rangle_{P_0} \sum_{f=1}^{N_{F,P_0}} \frac{\langle \vec{u}^{\star}_{P_0} + \vec{u}^{\star}_{P_{1,f}}, \vec{n}_f \rangle}{2} + \|\vec{n}_f\| \, h_{f,RHS,p} \frac{p^{\star}_{P_0} - p^{\star}_{P_{1,f}}}{2} \tag{77}$$

and

$$\Delta V_{P_0} \frac{\Delta u_{i,P_0}}{\Delta t} + \sum_{f=1}^{N_{F,P_0}} h_{f,LHS,u} \, n_{f,i} \frac{\langle \Delta \vec{u}_{P_0} - \Delta \vec{u}_{P_{1,f}}, \vec{e}_f \rangle}{2} =$$
$$\sum_{f=1}^{N_{F,P_0}} n_{f,i} \left(-\frac{1}{\langle \rho \rangle_{P_0}} \frac{p^{\star}_{P_0} + p^{\star}_{P_{1,f}} + p^{n+1}_{P_0} + p^{n+1}_{P_{1,f}}}{2} - h_{f,RHS,u} \frac{\langle \vec{u}^{\star}_{P_0} - \vec{u}^{\star}_{P_{1,f}}, \vec{e}_f \rangle}{2} \right) , \tag{78}$$

where the coefficients of the left hand side (LHS) and the right hand side (RHS) for pressure (i.e. $h_{f,LHS,p}$ and $h_{f,RHS,p}$) and velocity (i.e. $h_{f,LHS,u}$ and $h_{f,RHS,u}$) are given by

$$h_{f,LHS,p} = \left(1 - \frac{\phi_{P_0}}{2}\right) \frac{\nu_f}{\overline{\rho c}_f} \tag{79}$$

$$h_{f,RHS,p} = \frac{\nu_f}{\overline{\rho c}_f} + \left(1 - \phi_{P_0}\right) \frac{1}{\overline{\rho c}_f} \tag{80}$$

$$h_{f,LHS,u} = \frac{\overline{\rho c}_f}{\langle \rho \rangle_{P_0}} \left(-\phi_{P_0} \, \gamma + \left(1 - \phi_{P_0}\right) \nu_f \right) \tag{81}$$

$$h_{f,RHS,u} = \left(1 - \phi_{P_0}\right) \frac{\overline{\rho c}_f}{\langle \rho \rangle_{P_0}} \left(\nu_f + 1\right) \quad . \tag{82}$$

For the unstructured meshes which are of interest here we use the limiter function of [178]. The parameter of the limiter function is computed at time level $\star$ on the basis of pressure for Eq. (77) and velocity for Eq. (78).

3. Results

In the present section we present results obtained with the ICS-WAF method. We tested and validated this method extensively with numerous test cases. Using analytical solutions the formal order of accuracy is established in physical space and time. Furthermore, incompressible and compressible benchmark problems are computed including the lid-driven cavity problem, the two-dimensional Taylor-Green vortex, different Riemann problems, and the laminar boundary layer over a flat plate at different Mach numbers. The results for all of these test cases are discussed in the following sections. In addition, results for a standing wave are given to demonstrate the improvements of the ICS-WAF method over previous approaches [1,32]. At the end of this section the application of the ICS-WAF method to complex flows is presented.

3.1. Accuracy

To demonstrate the spatial accuracy of the present ICS-WAF method we consider an isentropic vortex at two different Mach numbers, namely 0.05 (case 1) and 0.5 (case 2). Details on the test case are given in [32]. The spatial error is plotted versus grid size in Fig. 7. Second order accuracy is obtained in space (see also Table 1). The temporal accuracy is investigated with the help of an isentropic acoustic wave at different flow speeds (case 1 at 0 m/s and case 2 at 20 m/s). Details on the setup are also provided in [32]. The results are summarized in Fig. 8 where plots of the temporal error versus time step size are shown. An order of two is found for large time steps which decreases slightly for smaller time steps due to the presence of other discretization errors (see also Table 2).

3.2. Riemann problems

To further assess the accuracy of the ICS-WAF method we investigate in this section Riemann problems for the Euler equations. As suggested in [152] we consider for this purpose three different Riemann problems. The initial conditions for these Riemann problems (denoted by RP1, RP2, and RP3) are summarized in Table 3. The solution of the first Riemann problem RP1 consists of two rarefactions and a stationary contact discontinuity. The second Riemann Problem is the so called Sod test case [179] and its solution is given by a left rarefaction, a contact discontinuity, and a right shock wave. For the third Riemann problem RP3 the solution consists of a left shock wave, a contact discontinuity, and a right shock wave. For all computations the monotone ICS-WAF scheme outlined

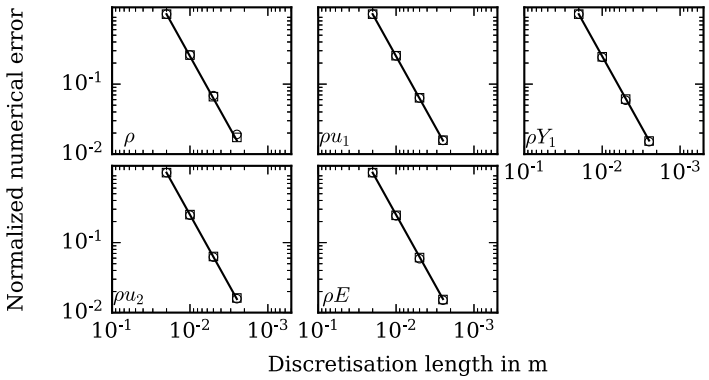

Fig. 7. Normalized numerical error of the transported variables over the discretization length for the isentropic vortex test cases 1 and 2. The magnitude of the errors for each variable is normalized with the magnitude of error on the coarsest grid for each variable. (——) nominal second order, (○) Mach number 0.05, (□) Mach number 0.5.

Table 1
Spatial convergence rate for isentropic vortex.

Mach number	Δx_1 in m	Normalized error					Convergence rate				
		ρ	ρu_1	ρu_2	ρE	ρY_1	ρ	ρu_1	ρu_2	ρE	ρY_1
0.05	2.0e-02	1.0e+00	1.0e+00	1.0e+00	1.0e+00	1.0e+00	-	-	-	-	-
0.05	1.0e-02	2.6e-01	2.5e-01	2.5e-01	2.4e-01	2.4e-01	1.9	2.0	2.0	2.1	2.1
0.05	5.0e-03	6.8e-02	6.3e-02	6.2e-02	5.9e-02	5.9e-02	1.9	2.0	2.0	2.0	2.0
0.05	2.5e-03	1.9e-02	1.6e-02	1.6e-02	1.5e-02	1.5e-02	1.8	2.0	2.0	2.0	2.0
0.5	2.0e-02	1.0e+00	1.0e+00	1.0e+00	1.0e+00	1.0e+00	-	-	-	-	-
0.5	1.0e-02	2.6e-01	2.5e-01	2.5e-01	2.5e-01	2.5e-01	1.9	2.0	2.0	2.0	2.0
0.5	5.0e-03	6.6e-02	6.4e-02	6.3e-02	6.1e-02	6.1e-02	2.0	2.0	2.0	2.0	2.0
0.5	2.5e-03	1.7e-02	1.6e-02	1.6e-02	1.5e-02	1.5e-02	1.9	2.0	2.0	2.0	2.0

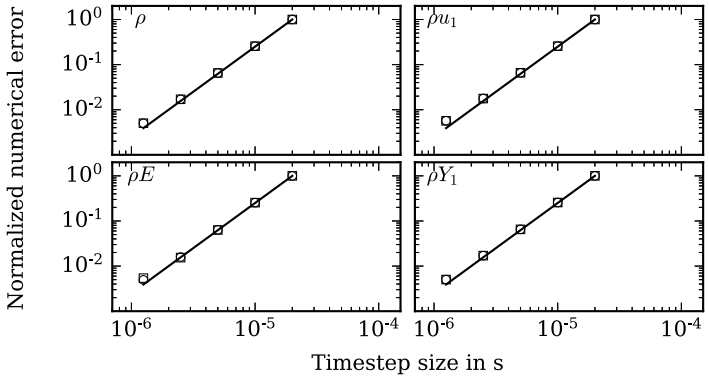

Fig. 8. Normalized numerical error of the transported variables over the time step for the isentropic acoustic wave cases 1 and 2. The magnitude of errors for each variable is normalized by the error at the largest time step. (——) nominal second order, (○) case 1, (□) case 2.

in Sec. 2.5 is used. An ideal gas is assumed with a constant heat capacity at constant pressure of 894.9 J/(kg K) and a specific gas constant of 288.3 J/(kg K) (the ratio of specific heats equals 1.4753). The computations are performed on hexahedral domain which extends from −0.05 m to 0.05 m in x_1 direction and from −50 µm to 50 µm in x_2 and x_3 directions. To obtain a one dimensional flow problem symmetry boundary conditions are prescribed at the boundary planes normal to the x_2 and x_3 directions. This domain is discretized with 3200 control volumes in x_1 direction and two control volumes in x_2 and x_3 direction, respectively. A time step size of $5 \cdot 10^{-9}$ s is used for solving Riemann problems RP1 and RP3 whereas a time steps size of $5 \cdot 10^{-8}$ s is used for solving RP2. Numerical results are compared to the exact solution at a time of 50 µs for RP1 and RP2 and 40 µs for RP3. The comparison between numerical and exact solution is given in Fig. 9 for RP1. An excellent agreement is found between both solutions for this Riemann problem. Likewise, a good agreement between exact and numerical solution is found for the Riemann problems RP2 and RP3 (cf. Figs. 10 and 11, respectively). It must be noted, however, that the ICS-WAF method is in general not well suited for capturing strong shock waves since it is based on the assumption that the wave speed equals the characteristic speed as outlined in Sec. 2.2.1. For the

Table 2
Temporal convergence rate for acoustic wave.

case	Δt in s	Normalized error				Convergence rate			
		ρ	ρu_1	ρE	ρY_1	ρ	ρu_1	ρE	ρY_1
1	2.0e-05	1.0e+00	1.0e+00	1.0e+00	1.0e+00	-	-	-	-
1	1.0e-05	2.6e-01	2.6e-01	2.6e-01	2.6e-01	2.0	2.0	2.0	2.0
1	5.0e-06	6.5e-02	6.6e-02	6.4e-02	6.5e-02	2.0	2.0	2.0	2.0
1	2.5e-06	1.7e-02	1.8e-02	1.6e-02	1.7e-02	1.9	1.9	2.0	1.9
1	1.3e-06	5.0e-03	5.7e-03	5.0e-03	5.0e-03	1.8	1.6	1.7	1.8
2	2.0e-05	1.0e+00	1.0e+00	1.0e+00	1.0e+00	-	-	-	-
2	1.0e-05	2.6e-01	2.6e-01	2.5e-01	2.6e-01	2.0	2.0	2.0	2.0
2	5.0e-06	6.5e-02	6.6e-02	6.3e-02	6.5e-02	2.0	2.0	2.0	2.0
2	2.5e-06	1.7e-02	1.8e-02	1.5e-02	1.7e-02	1.9	1.9	2.0	1.9
2	1.3e-06	5.0e-03	5.7e-03	5.4e-03	5.0e-03	1.8	1.6	1.5	1.8

Table 3
Initial conditions for Riemann problems.

Riemann problem	$x < 0$ m			$x \geq 0$ m		
	ρ in kg/m^3	p in bar	u_1 in m/s	ρ in kg/m^3	p in bar	u_1 in m/s
RP1	1.16	1	−210	1.16	1	210
RP2	1.16	1	0	0.92	0.8	0
RP3	1.16	1	40	0.116	1	0

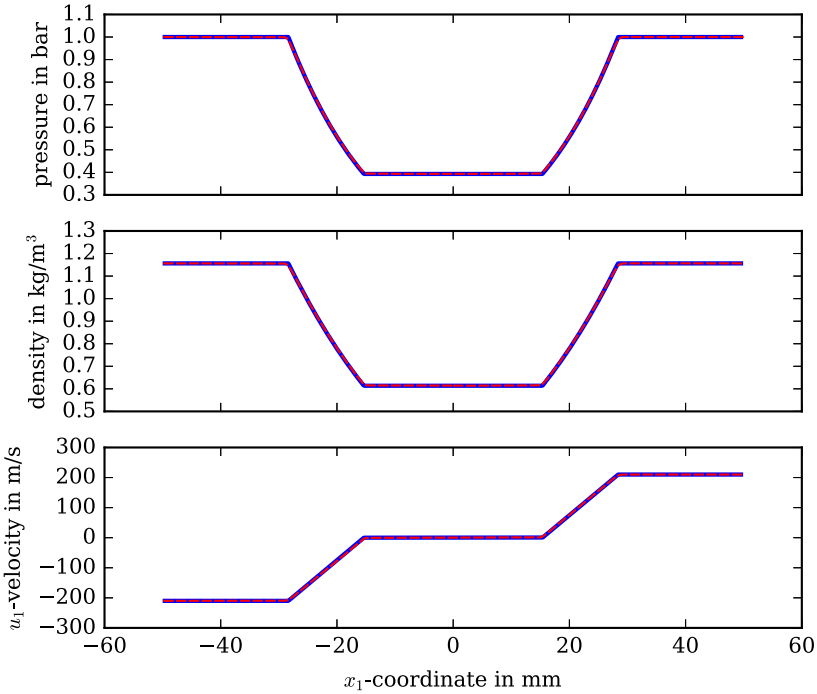

Fig. 9. Solution of Riemann problem RP1. (——) exact solution, (- - -) numerical solution of ICS-WAF method.

Riemann problems RP2 and RP3 given in Table 3 this condition is almost fulfilled since the ratio of pressures across a shock wave is close to one.

3.3. Low Mach number limit

In this section the asymptotic behavior of the ICS-WAF scheme in the low Mach number limit is investigated. As Mach number decreases the deviation from the incompressible limit in dimensionless pressure, dimensionless density, and dimensionless velocity divergence should decrease with the square of Mach number provided that acoustic perturbations are absent (see e.g. [137,139,180]).

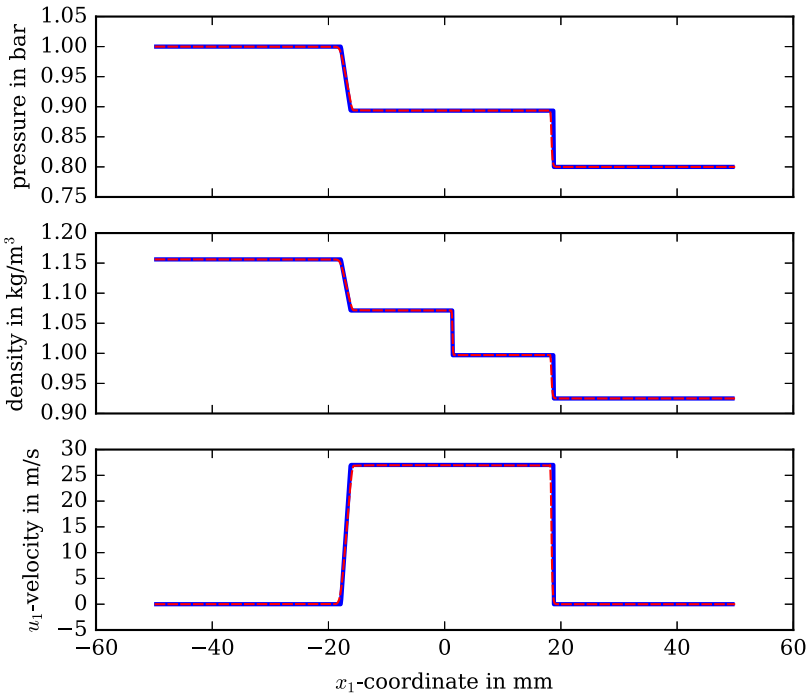

Fig. 10. Solution of Riemann problem RP2. (——) exact solution, (- - -) numerical solution of ICS-WAF method.

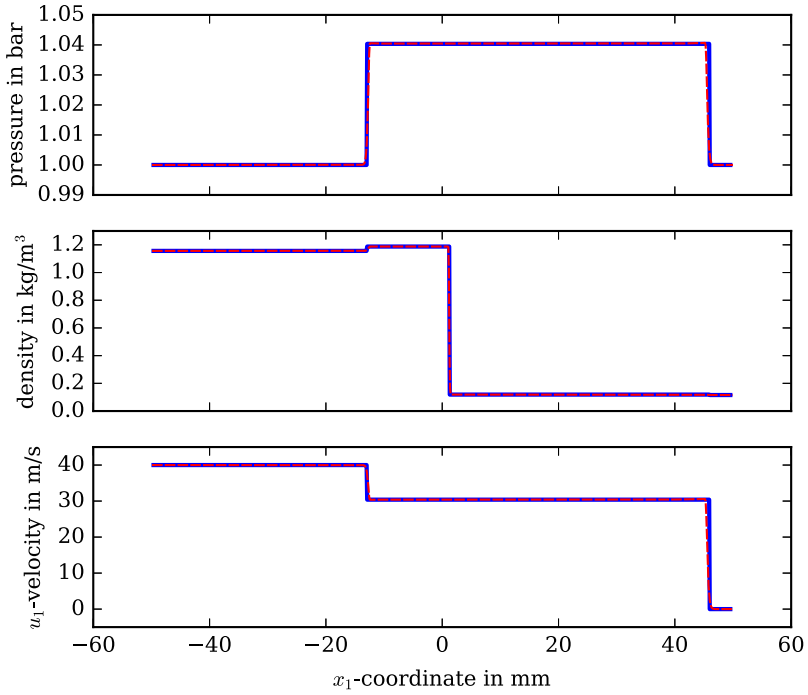

Fig. 11. Solution of Riemann problem RP3. (——) exact solution, (- - -) numerical solution of ICS-WAF method.

To demonstrate this behavior for the ICS-WAF scheme we perform a numerical experiment as proposed in [149] and compute a Taylor-Green vortex (TGV) for different Mach numbers. For each Mach number the deviation from the incompressible solution is evaluated. For the TGV the dimensionless solution for u_1 and u_2 velocities and relative pressure Δp in the incompressible limit is given by

Table 4
Physical parameters of Taylor-Green vortex.

$Ma_{0,TGV}$	$u_{0,TGV}$ in m/s	$\ell_{0,TGV}$ in mm	$\mu_{0,TGV}$ in µPa s	Re	Sr
0.1	35.72	10	500	8.26	1
0.01	3.572	1	5	8.26	1
0.001	0.3572	0.1	0.05	8.26	1

$$\check{u}_1 = u_1/u_{0,TGV} = -\cos\left(\frac{\pi}{2}\check{x}_1\right)\,\sin\left(\frac{\pi}{2}\check{x}_2\right)\,F(\check{t})\ , \tag{83}$$

$$\check{u}_2 = u_2/u_{0,TGV} = \sin\left(\frac{\pi}{2}\check{x}_1\right)\,\cos\left(\frac{\pi}{2}\check{x}_2\right)\,F(\check{t})\ , \tag{84}$$

$$\Delta\check{p} = \Delta p/(\rho_{0,TGV}\,u_{0,TGV}^2) = -\frac{1}{4}\left(\cos\left(\pi\check{x}_1\right)+\cos\left(\pi\check{x}_2\right)\right)\,F(\check{t})^2 \tag{85}$$

where the symbol $\check{\bullet}$ denotes dimensionless quantities. The function $F(\check{t})$ is defined as

$$F(\check{t}) = exp\left(-\frac{\pi^2\,\check{t}}{2\,Sr\,Re}\right) \tag{86}$$

in terms of the Strouhal number

$$Sr = \frac{\ell_{0,TGV}}{u_{0,TGV}\,t_{0,TGV}}$$

and the Reynolds number

$$Re = \frac{u_{0,TGV}\,\ell_{0,TGV}\,\rho_{0,TGV}}{\mu_{0,TGV}}\ .$$

Dimensionless time and space coordinates are defined as $\check{t} = t/t_{0,TGV}$ and $\check{x}_i = x_i/\ell_{0,TGV}$, respectively. $t_{0,TGV}$ and $\ell_{0,TGV}$ are reference time and length scales of the TGV. In the above equations $u_{0,TGV}$ denotes a reference velocity, $\rho_{0,TGV}$ a reference density, and $\mu_{0,TGV}$ the dynamic viscosity which is taken to be constant. The reference Mach number for the TGV is defined in terms of the reference speed of sound $c_{0,TGV}$ as

$$Ma_{0,TGV} = \frac{u_{0,TGV}}{c_{0,TGV}}\ .$$

In this study the reference Mach numbers 0.001, 0.01, and 0.1 are considered. To modify Mach number we keep the speed of sound $c_{0,TGV}$ constant and change the velocity $u_{0,TGV}$. In order to ensure similar solutions in the incompressible limit despite the change in $u_{0,TGV}$ the Strouhal number and the Reynolds number must be kept constant as the Mach number changes. To this end $\ell_{0,TGV}$ and $\mu_{0,TGV}$ are adjusted as summarized in Table 4. Furthermore, the Prandtl number is also kept constant at a value of 0.7 in the computations with the ICS-WAF scheme. For each computation the same reference pressure $P_{0,TGV} = 1000$ Pa as well as the same reference density $\rho_{0,TGV} = 0.011562$ kg/m^3 are used. With a specific gas constant of 288.3 J/(kg K) this corresponds to a gas temperature of 300 K and a speed of sound of $c_{0,TGV} = 357.2$ m/s (the ratio of specific heats equals 1.4753, the specific heat capacity at constant pressure equals 894.9 J/(kg K) and is taken to be constant). The computations are performed on a hexahedral domain which extends from -1 to 1 in dimensionless $\check{x}_1$ and $\check{x}_2$ directions and from -0.02 to 0.02 in dimensionless $\check{x}_3$ direction. It is discretized with 50 control volumes in $\check{x}_1$ and $\check{x}_2$ directions and two control volumes in $\check{x}_3$ direction. All computations are initialized with a constant density $\rho_{0,TGV}$ and velocities according to Eqs. (83) and (84). The initial pressure is the sum of the reference pressure $P_{0,TGV}$ and the relative pressure given in Eq. (85). The computations are run until $\check{t} = 1$ for $t_{0,TGV} = 0.00028$ s. At this point in time the velocity in the TGV has decayed about 45% from its initial value. All computations are run with an acoustic CFL of 0.001. For this numerical experiment it is found that a small acoustic CFL number is necessary to reduce the numerical errors sufficiently such that the correct scaling in velocity divergence at the smallest Mach number of 0.001 is obtained. At the end of the computation the L^2-norm of the deviation from the incompressible limit in dimensionless pressure, dimensionless density, and dimensionless velocity divergence, i.e. (Einstein notation)

$$\check{p} = \frac{p}{p_{0,TGV}}\ ,\quad \check{\rho} = \frac{\rho}{\rho_{0,TGV}}\ ,\quad \frac{\partial\check{u}_i}{\partial\check{x}_i} = \frac{\partial u_i}{\partial x_i}\,\frac{\ell_{0,TGV}}{u_{0,TGV}}$$

is evaluated. The results are summarized in Fig. 12 and Table 5. For the present numerical experiment the numerical solution of the ICS-WAF scheme approaches the incompressible limit with the square of Mach number, showing thus the expected scaling.

3.4. Lid-driven cavity

The laminar lid-driven cavity flow is a well known model problem which is often used to assess numerical flow solvers operating in viscous, low Mach number flow regimes. The problem consists of a cavity with a square cross section surrounded by no-slip walls.

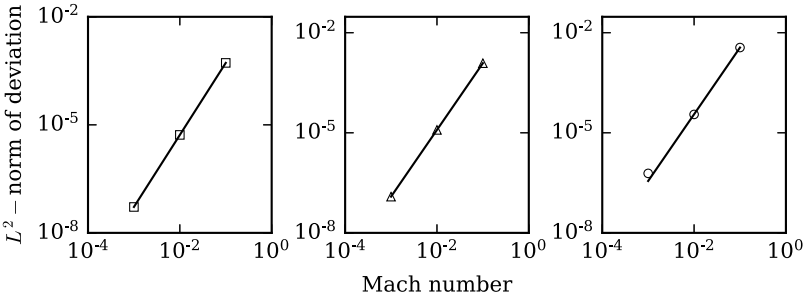

Fig. 12. Deviation from incompressible limit over Mach number for the Taylor-Green vortex. (——) nominal second order, (□) dimensionless density, (△) dimensionless pressure, (○) dimensionless velocity divergence.

Table 5
Convergence in Mach number $Ma_{0,\mathrm{TGV}}$ for Taylor green vortex. The deviations from the incompressible limit of dimensionless density, dimensionless pressure, and of dimensionless velocity divergence are given in the L^2-norm.

$Ma_{0,\mathrm{TGV}}$	Deviation			Convergence rate		
	$\check{\rho}$	$\check{p}$	$\sum_{i=1}^{3} \frac{\partial \check{u}_i}{\partial \check{x}_i}$	$\check{\rho}$	$\check{p}$	$\sum_{i=1}^{3} \frac{\partial \check{u}_i}{\partial \check{x}_i}$
1.0e-01	5.2e-04	1.2e-03	3.6e-03	-	-	-
1.0e-02	5.3e-06	1.2e-05	3.6e-05	2.0	2.0	2.0
1.0e-03	5.2e-08	1.2e-07	6.1e-07	2.0	2.0	1.8

As the upper wall moves, a shear driven flow is induced. Depending on the fluid properties as well as the velocity of the moving wall $u_{0,\mathrm{LDC}}$, different flows characterized by the Reynolds number

$$Re = \frac{u_{0,\mathrm{LDC}}\, \ell_{0,\mathrm{LDC}}\, \rho_{0,\mathrm{LDC}}}{\mu_{0,\mathrm{LDC}}}$$

can be defined. The parameter $\ell_{0,\mathrm{LDC}}$ is the characteristic length of the cavity whereas $\mu_{0,\mathrm{LDC}}$ is the dynamic viscosity (which is taken to be constant), and $\rho_{0,\mathrm{LDC}}$ the reference density. In the present work an ideal gas is assumed with constant specific heat capacity at constant pressure of 1009 J/(kg K) and a specific gas constant of 288.3 J/(kg K) (the ratio of specific heats equals 1.4). A reference length of 1 m is used here, the velocity of the moving wall is 1 m/s. Furthermore, a reference pressure of 7.14 bar and a reference density of 1 kg/m^3 is used. In this way a Mach number of 0.001 is obtained based on the velocity of the moving wall. The computational domain is hexahedral. It extends from 0 m to 1 m in x_1 and x_2 direction and from 0 m to 0.005 m in x_3 direction. Symmetry boundary conditions are prescribed at the boundary planes normal to the x_3 direction in order to obtain a two dimensional flow. The domain is discretized with an equally spaced grid which consists 202 control volumes in x_1 and x_2 direction, and two control volumes in x_3 direction. Three different Reynolds numbers ($Re = 100$, 1000, and 5000) are investigated. All simulations are run until a steady state solution is reached. The velocity components u_1 and u_2 are compared against the data published in [181]. The resulting velocities u_1 and u_2 are plotted in Fig. 13 along the center lines of the cavity at $x_1 = 0.5$ m and $x_2 = 0.5$ m. A good agreement between the data obtained from the ICS-WAF method and the data published in [181] is found in Fig. 13. This confirms that the ICS-WAF method works correctly for viscous, low Reynolds number flows at small Mach number.

3.5. Laminar boundary layer

For a further investigation of the ICS-WAF method in viscous flows the laminar boundary layer over a flat, isothermal plate is investigated here. The computational domain is shown schematically in Fig. 14. It extends from $x_1 = -700$ mm to $x_1 = 70$ mm and from $x_2 = 0$ mm to $x_2 = 700$ mm. Its extension in x_3 direction is 1 mm. The flat plate has a total length of 70 mm and is located along the lower boundary between $x_1 = 0$ mm to $x_1 = 70$ mm as indicated in Fig. 14. The computational domain is discretized with a structured mesh consisting of 263 control volumes in x_1 direction, 231 control volumes in x_2 direction, and two control volumes in x_3 direction. The height of the first cells along the wall is 0.5 μm, the growth rate of the control volumes normal to the wall is 5%. The aspect ratio in x_1 and x_2 direction increases for the control volumes at the wall from almost one at the tip of the plate to about 7000 at the end of the plate. Four different free stream Mach numbers Ma_∞, i.e. 0.1, 0.3, 0.6, and 0.9, are considered here. To provide a reference solution for the computations with the ICS-WAF method, the boundary layer equations for compressible flows are solved for these four Mach numbers. For this purpose the Levy-Lees transformation [182]

$$\vartheta = \int_0^{x_1} \rho_e \mu_e u_{1,e}\, d\tilde{x}_1 \tag{87}$$

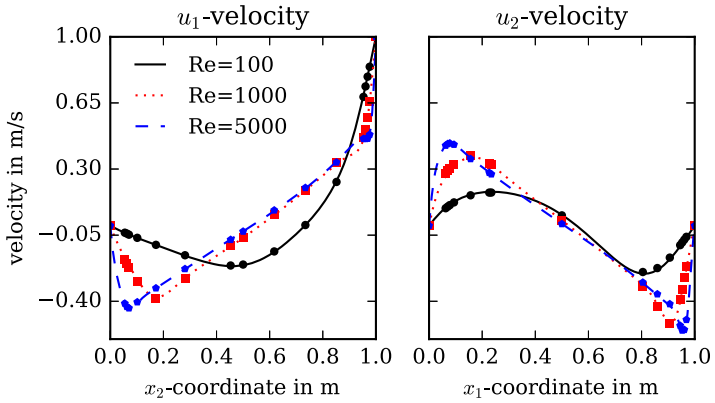

Fig. 13. Velocity u_1 and u_2 for the lid-driven cavity problem. Velocities are sampled along $x_1 = 0.5$ m for u_1 and along $x_2 = 0.5$ m for u_2. Lines represent the data of the ICS-WAF method whereas symbols represent the results from [181].

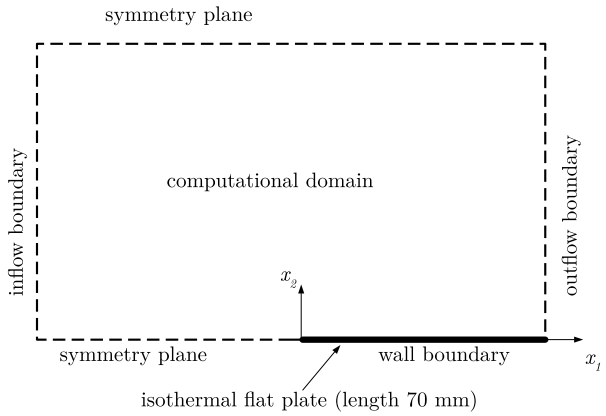

Fig. 14. Computational domain for solving laminar boundary layer flow over flat plate.

$$\psi = \frac{u_{1,e}}{\sqrt{2\vartheta}} \int_0^{x_2} \rho d\tilde{x}_2 \tag{88}$$

is used to transform the x_1, x_2 coordinates in ϑ, ψ coordinates as outlined in [183]. Here, ρ_e, μ_e, and $u_{1,e}$ denote the density, dynamic viscosity, and u_1-velocity at the edge of the boundary layer, respectively. The operator $\tilde{\bullet}$ denotes the variable of integration. With the help of Levy-Lees transformation the boundary layer equations are reduced to a set of two ordinary differential equations (see [183]). These equations are solved here numerically by using an iterative shooting technique. We assume an ideal gas with a constant dynamic viscosity of $7.5 \cdot 10^{-5}$ Pa s, a specific gas constant of 259.8 J/(kg K) (the ratio of specific heats equals 1.52, the specific heat capacity at constant pressure equals 760.5 J/(kg K) and is taken to be constant), and a Prandtl number of 0.7. Furthermore, we take the free stream temperature to be 300 K and the pressure to be 1 bar. The free stream velocities are 34.41 m/s, 103.23 m/s, 206.47 m/s, and 309.70 m/s for the Mach numbers of 0.1, 0.3, 0.6, and 0.9, respectively. Computational results of the ICS-WAF method are compared to the reference solution in Fig. 15. In this figure the similarity coordinate ψ is plotted versus temperature and u_1-velocity at $x_1 = 52.2$ mm. This location corresponds to length based Reynolds numbers of 30743, 92230, 184461, and 276691 for the Mach numbers 0.1, 0.3, 0.6, and 0.9. A good agreement between the ICS-WAF method and the reference solution is found for all Mach numbers. In particular, the increase of temperature within the boundary layer due to viscous dissipation is clearly visible.

3.6. Application to a standing wave

To illustrate the advantage of the combined ICS-WAF scheme over the original approach of [1] and later [32] we consider a one dimensional standing wave. Standing waves are frequently encountered (e.g. in thermo acoustic problems) and we choose here a test case which mimics closely the conditions described in [4]. The temperature of the gas is set to 2100 K and pressure is 6 bar and the composition of the gas is that of air (i.e. oxygen mass fraction of 23% and nitrogen mass fraction of 77%). Under these conditions the isentropic speed of sound is 945 m/s. We choose 0.189 m for the length of the domain which results in a Eigenfrequency of 2500 Hz. This is close to the frequency of the first longitudinal mode in [4]. We compute the evolution of this first longitudinal mode over time by solving the inviscid flow equations. The computation is conducted in a three-dimensional domain which has the shape

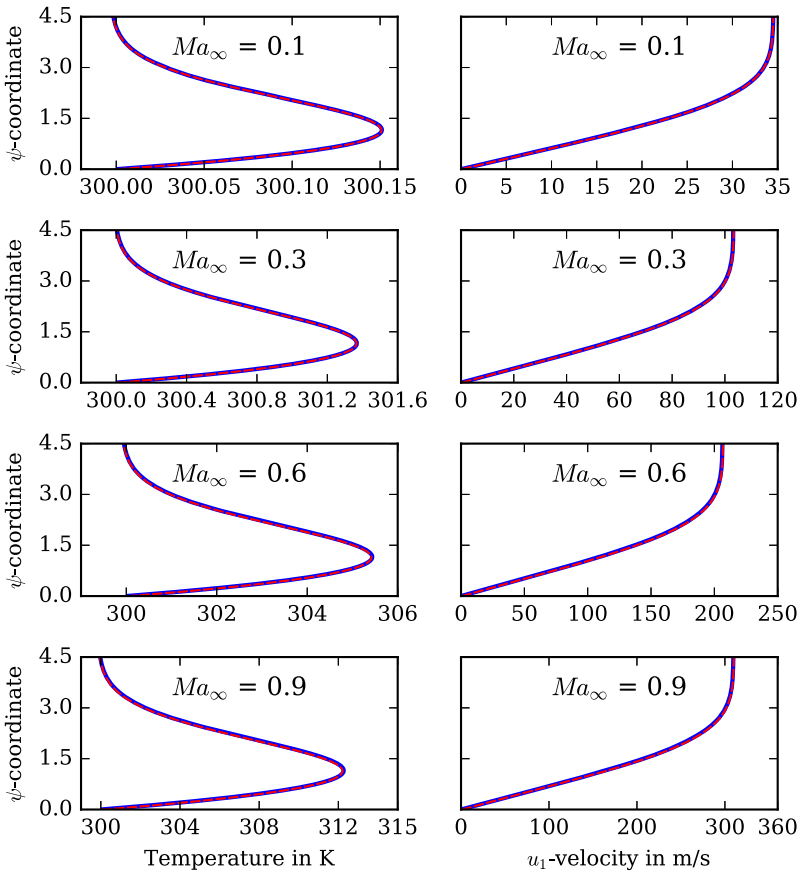

Fig. 15. Similarity variable ψ over temperature and u_1-velocity for free stream Mach numbers (Ma_∞) 0.1, 0.3, 0.6, and 0.9. Comparison between the ICS-WAF method (– – –) and the reference solution obtained from the boundary layer equations (——).

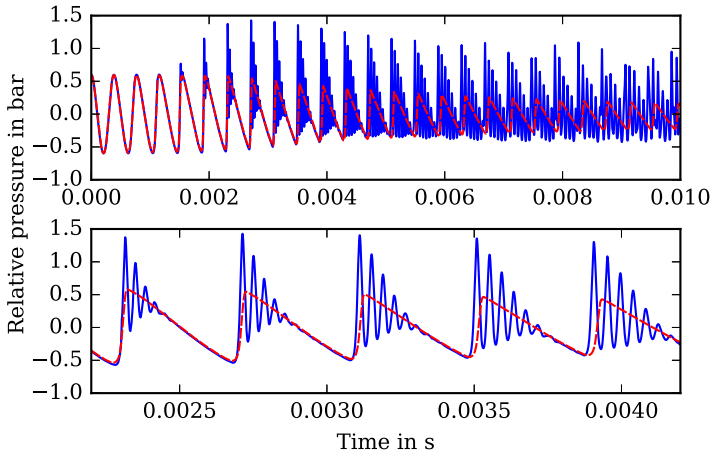

Fig. 16. Simulation of a standing wave. (——) ICS, (– – –) ICS-WAF.

of an elongated cuboid. The ends of this cuboid are fully reflecting, free slip walls whereas the two lateral dimensions are a pair of symmetry and periodic plains. The domain is discretized with 320 hexahedral cells (729 grid points), the computational time step size is 10^{-7} s. The initial amplitude of the pressure wave is set to 60 kPa which is a typical amplitude for the instabilities in the type of burners considered in [4]. For this amplitude nonlinear effects have a noticeable effect on the wave shape and wave steepening is observed as described in [184] and [33]. Furthermore, the wave is no longer isentropic and the wave amplitude decreases due to entropy production across the steep wave front [184]. This effect is reproduced very well by the combined ICS-WAF scheme as shown in Fig. 16. In this figure, the relative pressure at one of the walls is plotted versus time.

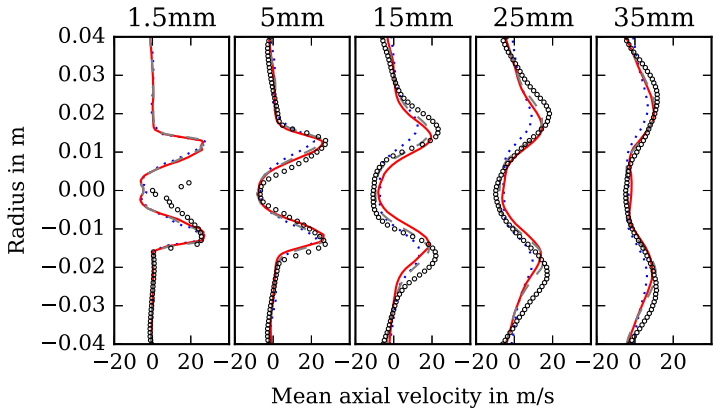

Fig. 17. Average axial velocity profiles of the isothermal swirl burner at different heights. (——) ICS-WAF, (— —) ICS, (·····) incompressible, (○) experiment.

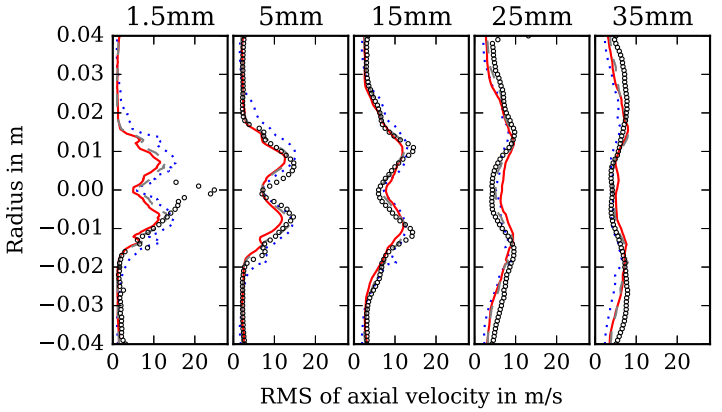

Fig. 18. Axial RMS velocity profiles of the isothermal swirl burner at different heights. (——) ICS-WAF, (— —) ICS, (·····) incompressible, (○) experiment.

For this computation it is necessary to use the monotone scheme in the acoustic step described in Sec. 2.5 (the parameter γ in Eq. (81) is set to 0.25). The possibility to enforce monotonicity in the ICS-WAF scheme is a clear advantage. The pressure correction equation used in the ICS scheme [32] on the other hand leads to the build up of an dispersive error which eventually renders the solution useless as shown in Fig. 16. Such build up of dispersive errors is also reported in the computations of [33]. This effect is not surprising since the original pressure correction relies on a purely central discretization in space. Hence, the present combined ICS-WAF scheme is a clear improvement of the original splitting scheme proposed in [32].

3.7. Application to complex flows

To demonstrate the applicability of the combined ICS-WAF method to practical problems this method is used in a LES of airflow through a swirl burner. This flow has been investigated experimentally and measurements for the root mean square (RMS) and average of each velocity component are provided [185]. The flow is isothermal (the air temperature is 320 K) at atmospheric pressure. This case is also investigated numerically in [1,32]. Since the Mach number of the flow in this burner is small simulations using an incompressible flow solver in ThetaCOM are also performed. For LES the wall-adapting local eddy-viscosity (WALE) model [186] is used as a subgrid-scale stress model. The time steps size is 0.1 µs which corresponds to a convective CFL number of 0.066 and an acoustic CFL number of 13. Computational results obtained with the ICS-WAF method are given in Figs. 17 to 22 for the average and RMS of velocities. In addition, results obtained with the incompressible solver and the ICS method [32] are also included in these figures. The profiles shown in these figures are evaluated in the center plane of the burner at different heights above the burner base plate (i.e. 1.5 mm, 5 mm, 15 mm, 25 mm, 35 mm). Similar to the results given in [1,32] some deviations between measurement and computations are observed upstream close to the exit of the swirler. Further downstream the overall agreement between simulation and experiment appears to be good. Both compressible solvers, i.e. the ICS-WAF method and the ICS method, appear to give very similar results. They show similar differences compared to the incompressible flow solver.

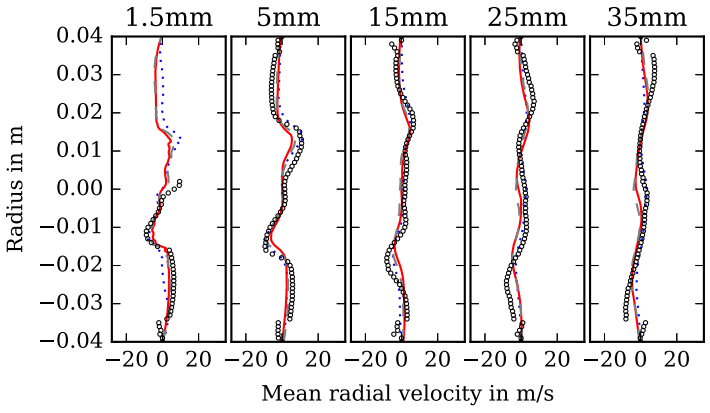

Fig. 19. Average radial velocity profiles of the isothermal swirl burner at different heights. (——) ICS-WAF, (— —) ICS, (·····) incompressible, (○) experiment.

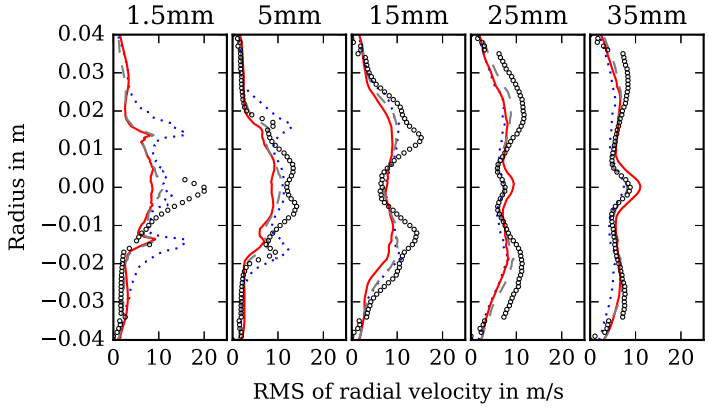

Fig. 20. Radial RMS velocity profiles of the isothermal swirl burner at different heights. (——) ICS-WAF, (— —) ICS, (·····) incompressible, (○) experiment.

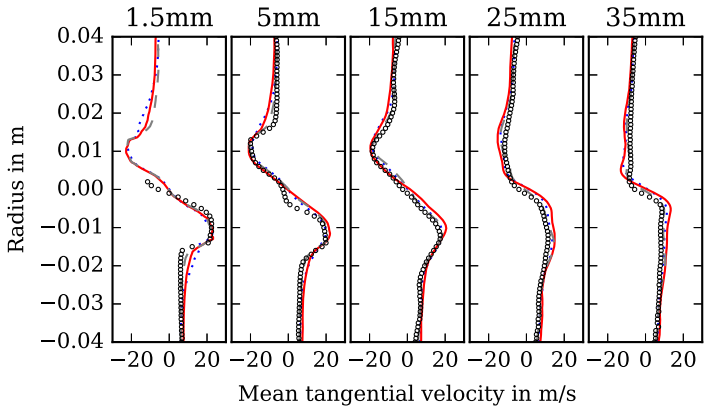

Fig. 21. Average tangential velocity profiles of the isothermal swirl burner at different heights. (——) ICS-WAF, (— —) ICS, (·····) incompressible, (○) experiment.

4. Summary

In this paper we present a novel approach for solving the acoustic step in the ICS scheme of [32]. This approach solves directly the hyperbolic system of equations in the acoustic step rather than relying on a pressure correction equation as in [1] and [32]. The solution method used here is based on the WAF method of [34]. In using this WAF method we assume equality of wave speed and characteristic speed which limits our approach to flows with pressure waves of comparatively small amplitude. For such flows this method is applicable to general unstructured meshes and it is not restricted by CFL conditions in computational time step size due to the use of Lerat's [169–171] implicit schemes. The approach is robust as demonstrated in Sec. 3.7 through the simulation of a complex flow and is second order accurate in physical space and time. An important aspect of this novel approach is that it opens an

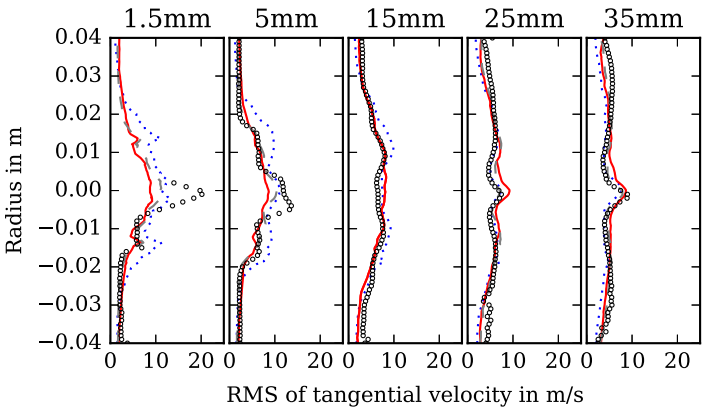

Fig. 22. Tangential RMS velocity profiles of the isothermal swirl burner at different heights. (——) ICS-WAF, (— —) ICS, (·····) incompressible, (○) experiment.

avenue for obtaining monotone solutions as shown in Sec. 2.5. This is important in many applications and is discussed here with the simple problem of a standing nonlinear wave (cf. Sec. 3.6). It is shown that earlier pressure correction based methods such as [32] are overly dispersive in this type of problem whereas the present approach is clearly superior. A further advantage of the method presented here is that it is possible to prove the stability of the approach (and subsequently of the entire splitting scheme) on the basis of the von Neumann stability analysis which is applied here to a linear model equation. To our knowledge such a proof of stability is still lacking for the pressure correction based methods of [1] and [32] which is a major disadvantage of these methods.

CRediT authorship contribution statement

A. Fiolitakis: Conceptualization, Methodology, Software, Validation, Visualization, Writing – original draft, Writing – review & editing. **M. Pries:** Software, Validation, Visualization, Writing – original draft, Writing – review & editing.

Declaration of competing interest

The authors declare that they have no known competing financial interests or personal relationships that could have appeared to influence the work reported in this paper.

Data availability

The authors do not have permission to share data.

Acknowledgement

We would like to thank apl. Prof. Dr. P. Gerlinger, Dr. P. Ess, and F. Setzwein, MSc. for the fruitful discussions on this work.

References

[1] V. Moureau, C. Bérat, H. Pitsch, An efficient semi-implicit compressible solver for large-eddy simulations, J. Comput. Phys. 226 (2007) 1256–1270, https://doi.org/10.1016/j.jcp.2007.05.035.
[2] R.H. Pletcher, J.C. Tannehill, D.A. Anderson, Computational Fluid Mechanics and Heat Transfer, 3rd ed., CRC Press, Boca Ration, London, New York, 2013.
[3] J.M. Lourier, M. Stöhr, B. Noll, S. Werner, A. Fiolitakis, Scale adaptive simulation of a thermoacoustic instability in a partially premixed lean swirl combustor, Combust. Flame 183 (2017) 343–357, https://doi.org/10.1016/j.combustflame.2017.02.024.
[4] F. Grimm, J.M. Lourier, O. Lammel, B. Noll, M. Aigner, A selective fast Fourier filtering approach applied to high frequency thermoacoustic instability analysis, in: Proceedings of ASME Turbo Expo 2017: Turbomachinery Technical Conference and Exposition, 2017, GT2017-63234.
[5] T. Kitano, K. Kaneko, R. Kurose, S. Komori, Large-eddy simulations of gas- and liquid-fueled combustion instabilities in back-step flows, Combust. Flame 170 (2016) 63–78, https://doi.org/10.1016/j.combustflame.2016.05.005.
[6] A.L. Pillai, R. Kurose, Numerical investigation of combustion noise in an open turbulent spray flame, Appl. Acoust. 133 (2018) 16–27, https://doi.org/10.1016/j.apacoust.2017.11.025.
[7] J. Nagao, A.L. Pillai, R. Kurose, Investigation of temporal variation of combustion instability intensity in a back step combustor using LES, J. Therm. Sci. Technol. 15 (2020), https://doi.org/10.1299/jtst.2020jtst0036 JTST0036.
[8] A.L. Pillai, J. Nagao, R. Awane, R. Kurose, Influences of liquid fuel atomization and flow rate fluctuations on spray combustion instabilities in a backward-facing step combustor, Combust. Flame 220 (2020) 337–356, https://doi.org/10.1016/j.combustflame.2020.06.031.
[9] T. Kitano, R. Kurose, S. Komori, Effects of internal pressure and inlet velocity disturbances of air and fuel droplets on spray combustion field, J. Therm. Sci. Technol. 8 (2013) 269–280, https://doi.org/10.1299/jtst.8.269.
[10] T. Kitano, T. Tsuji, R. Kurose, S. Komori, Effect of pressure oscillations on flashback characteristics in a turbulent channel flow, Energy Fuels 29 (2015) 6815–6822, https://doi.org/10.1021/acs.energyfuels.5b01687.
[11] R.N. Roy, M. Muto, R. Kurose, Direct numerical simulation of ignition of syngas (H_2/CO) mixtures with temperature and composition stratifications relevant to HCCI conditions, Int. J. Hydrog. Energy 42 (2017) 26152–26161, https://doi.org/10.1016/j.ijhydene.2017.08.182.

[12] U. Ahmed, A.L. Pillai, N. Chakraborty, R. Kurose, Statistical behavior of turbulent kinetic energy transport in boundary layer flashback of hydrogen-rich premixed combustion, Phys. Rev. Fluids 4 (2019) 103201, https://doi.org/10.1103/PhysRevFluids.4.103201.
[13] P. Yu, H. Watanabe, W. Zhang, R. Kurose, T. Kitagawa, Flamelet model for a three-feed non-premixed combustion system with a diluent stream: analysis and validation of quasi-two-dimensional flamelet (Q2DF) models, Energy Fuels 33 (2019) 4640–4650, https://doi.org/10.1021/acs.energyfuels.9b00764.
[14] R. Kai, A. Takahashi, R. Kurose, Numerical investigations of C1-C3 alkanes and H_2 premixed flame-wall interaction: effectiveness of insulation wall on heat loss reduction, J. Therm. Sci. Technol. 15 (2020), https://doi.org/10.1299/jtst.2020jtst0033 JTST0033.
[15] U. Ahmed, A.L. Pillai, N. Chakraborty, R. Kurose, Surface density function evolution and the influence of strain rates during turbulent boundary layer flashback of hydrogen-rich premixed combustion, Phys. Fluids 32 (2020) 055112, https://doi.org/10.1063/5.0004850.
[16] K. Konishi, R. Kai, R. Kurose, Unsteady flamelet modeling for N_2H_4/N_2O_4 flame accompanied by hypergolic ignition and thermal decomposition, Appl. Energy Combust. Sci. (2021) 100022, https://doi.org/10.1016/j.jaecs.2020.100022.
[17] H. Shehab, H. Watanabe, Y. Minamoto, R. Kurose, T. Kitagawa, Morphology and structure of spherically propagating premixed turbulent hydrogen - air flames, Combust. Flame 238 (2022) 111888, https://doi.org/10.1016/j.combustflame.2021.111888.
[18] P. Yu, R. Kurose, H. Watanabe, Investigation of the derivation and consistency of the quasi-two-dimensional flamelet models for non-premixed flames, Phys. Fluids 35 (2023) 015116, https://doi.org/10.1063/5.0134942.
[19] U. Ahmed, S.P. Malkeson, A.L. Pillai, N. Chakraborty, R. Kurose, Flame self-interaction during turbulent boundary layer flashback of hydrogen-rich premixed combustion, Phys. Rev. Fluids 8 (2023) 023202, https://doi.org/10.1103/PhysRevFluids.8.023202.
[20] R. Kai, T. Tokuoka, J. Nagao, A.L. Pillai, R. Kurose, LES flamelet modeling of hydrogen combustion considering preferential diffusion effect, Int. J. Hydrog. Energy 48 (2023) 11086–11101, https://doi.org/10.1016/j.ijhydene.2022.12.164.
[21] A.L. Pillai, R. Kurose, Combustion noise analysis of a turbulent spray flame using a hybrid DNS/APE-RF approach, Combust. Flame 200 (2019) 168–191, https://doi.org/10.1016/j.combustflame.2018.10.041.
[22] A.L. Pillai, S. Inoue, T. Shoji, S. Tachibana, T. Yokomori, R. Kurose, Investigation of combustion noise generated by an open lean-premixed H_2/air low-swirl flame using the hybrid LES/APE-RF framework, Combust. Flame 245 (2022) 112360, https://doi.org/10.1016/j.combustflame.2022.112360.
[23] J. Nagao, A.L. Pillai, T. Shoji, S. Tachibana, T. Yokomori, R. Kurose, Numerical investigation of wall effects on combustion noise from a lean-premixed hydrogen/air low-swirl flame, Phys. Fluids 35 (2023) 014109, https://doi.org/10.1063/5.0131974.
[24] T. Kitano, J. Nishio, R. Kurose, S. Komori, Effects of ambient pressure, gas temperature and combustion reaction on droplet evaporation, Combust. Flame 161 (2014) 551–564, https://doi.org/10.1016/j.combustflame.2013.09.009.
[25] R. Kai, R. Masuda, T. Ikedo, R. Kurose, Conjugate heat transfer analysis of methane/air premixed flame-wall interaction: a study on effect of wall material, Appl. Therm. Eng. 181 (2020) 115947, https://doi.org/10.1016/j.applthermaleng.2020.115947.
[26] A.L. Pillai, R. Kai, T. Murata, T. Ikedo, R. Masuda, R. Kurose, Numerical analysis of heat transfer characteristics of spray flames impinging on a wall under CI engine-like conditions, Combust. Flame 239 (2022) 111615, https://doi.org/10.1016/j.combustflame.2021.111615.
[27] P. Sarkar, G. Ghigliotti, J.P. Franc, M. Fivel, Fluid-structure modelling for material deformation during cavitation bubble collapse, J. Fluids Struct. 106 (2021) 103370, https://doi.org/10.1016/j.jfluidstructs.2021.103370.
[28] P. Sarkar, G. Ghigliotti, J.P. Franc, M. Fivel, Mechanism of material deformation during cavitation bubble collapse, J. Fluids Struct. 105 (2021) 103327, https://doi.org/10.1016/j.jfluidstructs.2021.103327.
[29] Y. Baba, K. Takahashi, Large-eddy simulation of convective boundary layer with density stratification, J. Meteorol. Soc. Jpn. Ser. II 89 (2011) 105–117, https://doi.org/10.2151/jmsj.2011-201.
[30] K. Matsuda, R. Onishi, K. Takahashi, Tree-crown-resolving large-eddy simulation coupled with three-dimensional radiative transfer model, J. Wind Eng. Ind. Aerodyn. 173 (2018) 53–66, https://doi.org/10.1016/j.jweia.2017.11.015.
[31] S. Wada, R. Kai, R. Kurose, A new semi-implicit pressure-based solver considering real gas effect, J. Comput. Phys. 501 (2024) 112782, https://doi.org/10.1016/j.jcp.2024.112782.
[32] M. Pries, A. Fiolitakis, P. Gerlinger, An implicit splitting scheme with characteristic boundary conditions for compressible reactive flows on unstructured grids, J. Comput. Appl. Math. 437 (2024) 115446, https://doi.org/10.1016/j.cam.2023.115446.
[33] J.D. Baum, J.N. Levine, Numerical techniques for solving nonlinear instability problems in solid rocket motors, AIAA J. 20 (1982) 955–961, https://doi.org/10.2514/3.7957.
[34] E.F. Toro, J.F. Clarke, A weighted average flux method for hyperbolic conservation laws, Proc. R. Soc. Lond. Ser. A, Math. Phys. Sci. 423 (1989) 401–418, https://doi.org/10.1098/rspa.1989.0062.
[35] J. Crank, P. Nicolson, A practical method for numerical evaluation of solutions of partial differential equations of the heat-conduction type, Math. Proc. Camb. Philos. Soc. 43 (1947) 50–67, https://doi.org/10.1017/S0305004100023197.
[36] J.G. Charney, R. Fjörtoft, J. Von Neumann, Numerical integration of the barotropic vorticity equation, Tellus 2 (1950) 237–254, https://doi.org/10.1111/j.2153-3490.1950.tb00336.x.
[37] S. Abarbanel, P. Duth, D. Gottlieb, Splitting methods for low Mach number Euler and Navier-Stokes equations, Comput. Fluids 17 (1989) 1–12, https://doi.org/10.1016/0045-7930(89)90003-0.
[38] T. Yabe, P. Wang, Unified numerical procedure for compressible and incompressible fluid, J. Phys. Soc. Jpn. 60 (1991) 2105–2108, https://doi.org/10.1143/JPSJ.60.2105.
[39] S.Y. Yoon, T. Yabe, The unified simulation for incompressible and compressible flow by the predictor-corrector scheme based on the CIP method, Comput. Phys. Commun. 119 (1999) 149–158, https://doi.org/10.1016/S0010-4655(99)00192-7.
[40] F. Xiao, Unified formulation for compressible and incompressible flows by using multi-integrated moments I: one-dimensional inviscid compressible flow, J. Comput. Phys. 195 (2004) 629–654, https://doi.org/10.1016/j.jcp.2003.10.014.
[41] F. Xiao, R. Akoh, S. Ii, Unified formulation for compressible and incompressible flows by using multi-integrated moments II: multi-dimensional version for compressible and incompressible flows, J. Comput. Phys. 213 (2006) 31–56, https://doi.org/10.1016/j.jcp.2005.08.002.
[42] S.Y. Kadioglu, M. Sussman, Adaptive solution techniques for simulating underwater explosions and implosions, J. Comput. Phys. 227 (2008) 2083–2104, https://doi.org/10.1016/j.jcp.2007.10.019.
[43] N. Kwatra, J. Su, J.T. Gretarsson, R. Fedkiw, A method for avoiding the acoustic time step restriction in compressible flow, J. Comput. Phys. 228 (2009) 4146–4161, https://doi.org/10.1016/j.jcp.2009.02.027.
[44] C. Chalons, M. Girardin, S. Kokh, An all-regime Lagrange-projection like scheme for the gas dynamics equations on unstructured meshes, Commun. Comput. Phys. 20 (2016) 188–233, https://doi.org/10.4208/cicp.260614.061115a.
[45] M.F.P. ten Eikelder, F. Daude, B. Koren, A.S. Tijsseling, An acoustic-convective splitting-based approach for the Kapila two-phase flow model, J. Comput. Phys. 331 (2017) 188–208, https://doi.org/10.1016/j.jcp.2016.11.031.
[46] D. Iampietro, F. Daude, P. Galon, J.-M. Herard, A Mach-sensitive splitting approach for Euler-like systems, ESAIM: Math. Model. Numer. Anal. 52 (2018) 207–253, https://doi.org/10.1051/m2an/2017063.
[47] D. Modesti, S. Pirozzoli, An efficient semi-implicit solver for direct numerical simulation of compressible flows at all speeds, J. Sci. Comput. 75 (2018) 308–331, https://doi.org/10.1007/s10915-017-0534-4.
[48] D. Iampietro, F. Daude, P. Galon, A low-diffusion self-adaptive flux-vector splitting approach for compressible flows, Comput. Fluids 206 (2020) 104586, https://doi.org/10.1016/j.compfluid.2020.104586.

[49] F. Bouchut, E. Franck, L. Navoret, A low cost semi-implicit low-Mach relaxation scheme for the full Euler equations, J. Sci. Comput. 83 (2020) 24, https://doi.org/10.1007/s10915-020-01206-z.
[50] R. Bourgeois, P. Tremblin, S. Kokh, T. Padioleau, Recasting an operator splitting solver into a standard finite volume flux-based algorithm. The case of a Lagrange-projection-type method for gas dynamics, J. Comput. Phys. 496 (2024), https://doi.org/10.1016/j.jcp.2023.112594.
[51] E.F. Toro, M.E. Vazquez-Cendon, Flux splitting schemes for the Euler equations, Comput. Fluids 70 (2012) 1–12, https://doi.org/10.1016/j.compfluid.2012.08.023.
[52] E.F. Toro, C.E. Castro, B.J. Lee, A novel numerical flux for the 3D Euler equations with general equation of state, J. Comput. Phys. 303 (2015) 80–94, https://doi.org/10.1016/j.jcp.2015.09.037.
[53] E. Turkel, Preconditioned methods for solving the incompressible and low speed compressible equations, J. Comput. Phys. 72 (1987) 277–298, https://doi.org/10.1016/0021-9991(87)90084-2.
[54] E. Turkel, Review of preconditioning methods for fluid dynamics, Appl. Numer. Math. 12 (1993) 257–284, https://doi.org/10.1016/0168-9274(93)90122-8.
[55] D. Choi, C.L. Merkle, Application of time-iterative schemes to incompressible flow, AIAA J. 23 (1985) 1518–1524, https://doi.org/10.2514/3.9119.
[56] Y.H. Choi, C.L. Merkle, The application of preconditioning in viscous flows, J. Comput. Phys. 105 (1993) 207–223, https://doi.org/10.1006/jcph.1993.1069.
[57] B. van Leer, W.T. Lee, P. Roe, Characteristic time-stepping or local preconditioning of the Euler equations, in: Proceedings of the 10th Computational Fluid Dynamics Conference, 1991, GT2017-63234.
[58] E. Turkel, Preconditioning techniques in computational fluid dynamics, Annu. Rev. Fluid Mech. 31 (1999) 385–416, https://doi.org/10.1146/annurev.fluid.31.1.385.
[59] J.M. Weiss, W.A. Smith, Preconditioning applied to variable and constant density flows, AIAA J. 33 (1995) 2050–2057, https://doi.org/10.2514/3.12946.
[60] W.R. Briley, L.K. Taylor, D.L. Whitfield, High-resolution viscous flow simulations at arbitrary Mach number, J. Comput. Phys. 184 (2003) 79–105, https://doi.org/10.1016/S0021-9991(02)00018-9.
[61] C.C. Rossow, Efficient computation of compressible and incompressible flows, J. Comput. Phys. 220 (2007) 879–899, https://doi.org/10.1016/j.jcp.2006.05.034.
[62] Y. Colin, H. Deniau, J.F. Boussuge, A robust low speed preconditioning formulation for viscous flow computations, Comput. Fluids 47 (2011) 1–15, https://doi.org/10.1016/j.compfluid.2011.01.015.
[63] H. Park, R.R. Nourgaliev, R.C. Martineau, D.A. Knoll, On physics-based preconditioning of the Navier–Stokes equations, J. Comput. Phys. 228 (2009) 9131–9146, https://doi.org/10.1016/j.jcp.2009.09.015.
[64] F. Rieper, A low-Mach number fix for Roe's approximate Riemann solver, J. Comput. Phys. 230 (2011) 5263–5287, https://doi.org/10.1016/j.jcp.2011.03.025.
[65] H. Yu, Z. Tian, F. Yang, H. Li, A numerical method for incompressible and compressible flow problems with smooth solutions, Math. Probl. Eng. 2020 (2020) 7451240, https://doi.org/10.1155/2020/7451240.
[66] D. Sun, C. Yan, F. Qu, R. Du, A robust flux splitting method with low dissipation for all-speed flows, Int. J. Numer. Methods Fluids 84 (2017) 3–18, https://doi.org/10.1002/fld.4337.
[67] S. Chen, F. Cai, X. Xiang, Z. Gao, C. Yan, A low-diffusion robust flux splitting scheme towards wide-ranging Mach number flows, Chin. J. Aeronaut. 34 (2021) 628–641, https://doi.org/10.1016/j.cja.2020.12.010.
[68] L. Hu, S. Tan, L. Li, H. Yuan, An accurate, robust and efficient convection-pressure flux splitting scheme for compressible Euler flows, J. Comput. Phys. 493 (2023) 112505, https://doi.org/10.1016/j.jcp.2023.112505.
[69] R. Frolov, An efficient algorithm for the multicomponent compressible Navier-Stokes equations in low- and high-Mach number regimes, Comput. Fluids 178 (2019) 15–40, https://doi.org/10.1016/j.compfluid.2018.10.001.
[70] Y.-L. Yoo, H.-G. Sung, A hybrid AUSM scheme (HAUS) for multi-phase flows with all Mach numbers, Comput. Fluids 227 (2021) 105050, https://doi.org/10.1016/j.compfluid.2021.105050.
[71] C. Berthon, C. Klingenberg, M. Zenk, An all Mach number relaxation upwind scheme, SMAI J. Comput. Math. 6 (2020) 1–31, https://doi.org/10.5802/smai-jcm.60.
[72] S. Busto, M. Dumbser, I. Peshkov, E. Romenski, On thermodynamically compatible finite volume schemes for continuum mechanics, SIAM J. Sci. Comput. 44 (2022) A1723–A1751, https://doi.org/10.1137/21M1417508.
[73] M. Feistauer, V. Kucera, On a robust discontinuous Galerkin technique for the solution of compressible flow, J. Comput. Phys. 224 (2007) 208–221, https://doi.org/10.1016/j.jcp.2007.01.035.
[74] M. Feistauer, V. Dolejsi, V. Kucera, On the discontinuous Galerkin method for the simulation of compressible flow with wide range of Mach numbers, Comput. Vis. Sci. 10 (2007) 17–27, https://doi.org/10.1007/s00791-006-0051-8.
[75] F. Bassi, C. De Bartolo, R. Hartmann, A. Nigro, A discontinuous Galerkin method for inviscid low Mach number flows, J. Comput. Phys. 228 (2009) 3996–4011, https://doi.org/10.1016/j.jcp.2009.02.021.
[76] M. Feistauer, V. Kucera, J. Prokopova, Discontinuous Galerkin solution of compressible flow in time-dependent domains, Math. Comput. Simul. 80 (2010) 1612–1623, https://doi.org/10.1016/j.matcom.2009.01.020.
[77] A. Nigro, C. De Bartolo, R. Hartmann, F. Bassi, Discontinuous Galerkin solution of preconditioned Euler equations for very low Mach number flows, Int. J. Numer. Methods Fluids 63 (2010) 449–467, https://doi.org/10.1002/fld.2083.
[78] M. Feistauer, J. Cesenek, V. Kucera, Discontinuous Galerkin method - a robust solver for compressible flow, Notes Numer. Fluid Mech. Multidiscipl. Des. 120 (2013) 143–160, https://doi.org/10.1007/978-3-642-33221-0_9.
[79] A. Nigro, S. Renda, C. De Bartolo, R. Hartmann, F. Bassi, A high-order accurate discontinuous Galerkin finite element method for laminar low Mach number flows, Int. J. Numer. Methods Fluids 72 (2013) 43–68, https://doi.org/10.1002/fld.3732.
[80] A. Nigro, A. Ghidoni, S. Rebay, F. Bassi, Modified extended BDF scheme for the discontinuous Galerkin solution of unsteady compressible flows, Int. J. Numer. Methods Fluids 76 (2014) 549–574, https://doi.org/10.1002/fld.3944.
[81] F. Bassi, L. Botti, A. Colombo, A. Ghidoni, F. Massa, Linearly implicit Rosenbrock-type Runge–Kutta schemes applied to the discontinuous Galerkin solution of compressible and incompressible unsteady flows, Comput. Fluids 118 (2015) 305–320, https://doi.org/10.1016/j.compfluid.2015.06.007.
[82] A. Nigro, C. De Bartolo, A. Crivellini, M. Franciolini, A. Colombo, F. Bassi, A low-dissipation DG method for the under-resolved simulation of low Mach number turbulent flows, Comput. Math. Appl. 77 (2019) 1739–1755, https://doi.org/10.1016/j.camwa.2018.09.049.
[83] W. Boscheri, M. Dumbser, E. Gaburro, Continuous finite element subgrid basis functions for discontinuous Galerkin schemes on unstructured polygonal Voronoi meshes, Commun. Comput. Phys. 32 (2022) 259–298, https://doi.org/10.4208/cicp.OA-2021-0235.
[84] J. Zeifang, J. Schütz, Implicit two-derivative deferred correction time discretization for the discontinuous Galerkin method, J. Comput. Phys. 464 (2022) 111353, https://doi.org/10.1016/j.jcp.2022.111353.
[85] K. Kaiser, J. Schütz, A high-order method for weakly compressible flows, Commun. Comput. Phys. 22 (2017) 1150–1174, https://doi.org/10.4208/cicp.OA-2017-0028.
[86] J. Zeifang, K. Kaiser, A. Beck, J. Schütz, C.-D. Munz, Efficient high-order discontinuous Galerkin computations of low Mach number flows, Commun. Appl. Math. Comput. Sci. 13 (2018) 243–270, https://doi.org/10.2140/CAMCOS.2018.13.243.
[87] J. Zeifang, J. Schütz, K. Kaiser, A. Beck, M. Lukacova-Medvid'ova, S. Noelle, A novel full-Euler low Mach number IMEX splitting, Commun. Comput. Phys. 27 (2020) 292–320, https://doi.org/10.4208/cicp.OA-2018-0270.
[88] G. Orlando, P.F. Barbante, L. Bonaventura, An efficient IMEX-DG solver for the compressible Navier-Stokes equations for non-ideal gases, J. Comput. Phys. 471 (2022) 111653, https://doi.org/10.1016/j.jcp.2022.111653.

[89] X. Meng, Y. Xu, Adaptive local discontinuous Galerkin methods with semi-implicit time discretizations for the Navier-Stokes equations, Adv. Aerodyn. 4 (2022) 22, https://doi.org/10.1186/s42774-022-00110-4.
[90] S. Noelle, G. Bispen, K.R. Arun, M. Lukacova-Medvimova, C.-D. Munz, A weakly asymptotic preserving low Mach number scheme for the Euler equations of gas dynamics, SIAM J. Sci. Comput. 36 (2014) B989–B1024, https://doi.org/10.1137/120895627.
[91] K. Kaiser, J. Schütz, R. Schöbel, S. Noelle, A new stable splitting for the isentropic Euler equations, J. Sci. Comput. 70 (2017) 1390–1407, https://doi.org/10.1007/s10915-016-0286-6.
[92] G. Bispen, M. Lukacova-Medvid'ova, L. Yelash, Asymptotic preserving IMEX finite volume schemes for low Mach number Euler equations with gravitation, J. Comput. Phys. 335 (2017) 222–248, https://doi.org/10.1016/j.jcp.2017.01.020.
[93] S. Avgerinos, F. Bernard, A. Iollo, G. Russo, Linearly implicit all Mach number shock capturing schemes for the Euler equations, J. Comput. Phys. 393 (2019) 278–312, https://doi.org/10.1016/j.jcp.2019.04.020.
[94] S. Boscarino, G. Russo, L. Scandurra, All Mach number second order semi-implicit scheme for the Euler equations of gas dynamics, J. Sci. Comput. 77 (2018) 850–884, https://doi.org/10.1007/s10915-018-0731-9.
[95] G. Dimarco, R. Loubere, V. Michel-Dansac, M.-H. Vignal, Second-order implicit-explicit total variation diminishing schemes for the Euler system in the low Mach regime, J. Comput. Phys. 372 (2018) 178–201, https://doi.org/10.1016/j.jcp.2018.06.022.
[96] S. Boscarino, J.-M. Qiu, G. Russo, T. Xiong, A high order semi-implicit IMEX WENO scheme for the all-Mach isentropic Euler system, J. Comput. Phys. 392 (2019) 594–618, https://doi.org/10.1016/j.jcp.2019.04.057.
[97] K.R. Arun, S. Samantaray, Asymptotic preserving low Mach number accurate IMEX finite volume schemes for the isentropic Euler equations, J. Sci. Comput. 82 (2020) 35, https://doi.org/10.1007/s10915-020-01138-8.
[98] Y. Jiang, X. Chen, X. Zhang, T. Xiong, S. Zhou, High order semi-implicit weighted compact nonlinear scheme for the all-Mach isentropic Euler system, Adv. Aerodyn. 2 (2020) 27, https://doi.org/10.1186/s42774-020-00052-9.
[99] W. Boscheri, G. Dimarco, R. Loubere, M. Tavelli, M.H. Vignal, A second order all Mach number IMEX finite volume solver for the three dimensional Euler equations, J. Comput. Phys. 415 (2020) 109486, https://doi.org/10.1016/j.jcp.2020.109486.
[100] A. Thomann, G. Puppo, C. Klingenberg, An all speed second order well-balanced IMEX relaxation scheme for the Euler equations with gravity, J. Comput. Phys. 420 (2020) 109723, https://doi.org/10.1016/j.jcp.2020.109723.
[101] A. Thomann, M. Zenk, G. Puppo, C. Klingenberg, An all speed second order IMEX relaxation scheme for the Euler equations, Commun. Comput. Phys. 28 (2020) 591–620, https://doi.org/10.4208/CICP.OA-2019-0123.
[102] V. Michel-Dansac, A. Thomann, TVD-MOOD schemes based on implicit-explicit time integration, Appl. Math. Comput. 433 (2022) 127397, https://doi.org/10.1016/j.amc.2022.127397.
[103] Y.-Q. Jiang, S.-G. Zhou, Y.-G. Hu, X. Zhang, High order semi-implicit weighted compact nonlinear scheme for the full compressible Euler system at all Mach numbers, Comput. Math. Appl. 109 (2022) 125–139, https://doi.org/10.1016/j.camwa.2022.01.020.
[104] S. Boscarino, J. Qiu, G. Russo, T. Xiong, High order semi-implicit WENO schemes for all-Mach full Euler system of gas dynamics, SIAM J. Sci. Comput. 44 (2022) B368–B394, https://doi.org/10.1137/21M1424433.
[105] M. Lukacova-Medvid'ova, I. Peshkov, A. Thomann, An implicit-explicit solver for a two-fluid single-temperature model, J. Comput. Phys. 498 (2024) 112696, https://doi.org/10.1016/j.jcp.2023.112696.
[106] W. Boscheri, L. Pareschi, High order pressure-based semi-implicit IMEX schemes for the 3D Navier-Stokes equations at all Mach numbers, J. Comput. Phys. 434 (2021) 110206, https://doi.org/10.1016/j.jcp.2021.110206.
[107] W. Boscheri, G. Dimarco, M. Tavelli, An efficient second order all Mach finite volume solver for the compressible Navier-Stokes equations, Comput. Methods Appl. Mech. Eng. 374 (2021) 113602, https://doi.org/10.1016/j.cma.2020.113602.
[108] Y.-Q. Jiang, S.-G. Zhou, X. Zhang, Y.-G. Hu, High order all-speed semi-implicit weighted compact nonlinear scheme for the isentropic Navier-Stokes equations, J. Comput. Appl. Math. 411 (2022) 114272, https://doi.org/10.1016/j.cam.2022.114272.
[109] M. Moghadas Khorasani, M.H. Djavareshkian, Enhancing accuracy and efficiency: a novel implicit-explicit approach for fluid dynamics simulation, Phys. Fluids 36 (2024) 036113, https://doi.org/10.1063/5.0193083.
[110] R.I. Issa, A.D. Gosman, A.P. Watkins, The computation of compressible and incompressible recirculating flows by a non-iterative implicit scheme, J. Comput. Phys. 62 (1986) 66–82, https://doi.org/10.1016/0021-9991(86)90100-2.
[111] J.P. van Doormaal, G.D. Raithby, B.H. McDonald, The segregated approach to predicting viscous compressible fluid flows, in: Proceedings of the Turbo Expo: Power for Land, Sea, and Air, vol. 1, 1986, 86-GT-196.
[112] K.C. Karki, S.V. Patankar, Pressure based calculation procedure for viscous flows at all speeds in arbitrary configurations, AIAA J. 27 (1989) 1167–1174, https://doi.org/10.2514/3.10242.
[113] W. Shyy, M.H. Chen, C.S. Sun, Pressure-based multigrid algorithm for flow at all speeds, AIAA J. 30 (1992) 2660–2669, https://doi.org/10.2514/3.11282.
[114] I. Demirdzic, Z. Lilek, M. Peric, A collocated finite volume method for predicting flows at all speeds, Int. J. Numer. Methods Fluids 16 (1993) 1029–1050, https://doi.org/10.1002/fld.1650161202.
[115] S.M.H. Karimian, G.E. Schneider, Pressure-based control-volume finite element method for flow at all speeds, AIAA J. 33 (1995) 1611–1618, https://doi.org/10.2514/3.12700.
[116] H. Bijl, P. Wesseling, A unified method for computing incompressible and compressible flows in boundary-fitted coordinates, J. Comput. Phys. 141 (1998) 153–173, https://doi.org/10.1006/jcph.1998.5914.
[117] P. Colella, K. Pao, A projection method for low speed flows, J. Comput. Phys. 149 (1999) 245–269, https://doi.org/10.1006/jcph.1998.6152.
[118] F. Nicoud, Conservative high-order finite-difference schemes for low-Mach number flows, J. Comput. Phys. 158 (2000) 71–97, https://doi.org/10.1006/jcph.1999.6408.
[119] F. Moukalled, M. Darwish, A high-resolution pressure-based algorithm for fluid flow at all speeds, J. Comput. Phys. 168 (2001) 101–130, https://doi.org/10.1006/jcph.2000.6683.
[120] C. Wall, C.D. Pierce, P. Moin, A semi-implicit method for resolution of acoustic waves in low Mach number flows, J. Comput. Phys. 181 (2002) 545–563, https://doi.org/10.1006/jcph.2002.7141.
[121] D.R. van der Heul, C. Vuik, P. Wesseling, A conservative pressure-correction method for flow at all speeds, Comput. Fluids 32 (2003) 1113–1132, https://doi.org/10.1016/S0045-7930(02)00086-5.
[122] Y. Hou, K. Mahesh, A robust, colocated, implicit algorithm for direct numerical simulation of compressible, turbulent flows, J. Comput. Phys. 205 (2005) 205–221, https://doi.org/10.1016/j.jcp.2004.10.039.
[123] Z.J. Chen, A.J. Przekwas, A coupled pressure-based computational method for incompressible/compressible flows, J. Comput. Phys. 229 (2010) 9150–9165, https://doi.org/10.1016/j.jcp.2010.08.029.
[124] P. Degond, M. Tang, All speed scheme for the low Mach number limit of the isentropic Euler equations, Commun. Comput. Phys. 10 (2011) 1–31, https://doi.org/10.4208/cicp.210709.210610a.
[125] F. Cordier, P. Degond, A. Kumbaro, An asymptotic-preserving all-speed scheme for the Euler and Navier-Stokes equations, J. Comput. Phys. 231 (2012) 5685–5704, https://doi.org/10.1016/j.jcp.2012.04.025.
[126] J. Haack, S. Jin, J.-G. Liu, An all-speed asymptotic-preserving method for the isentropic Euler and Navier-Stokes equations, Commun. Comput. Phys. 12 (2012) 955–980, https://doi.org/10.4208/cicp.250910.131011a.

[127] M. Darwish, F. Moukalled, A fully coupled Navier-Stokes solver for fluid flow at all speeds, Numer. Heat Transf., Part B, Fundam. 65 (2014) 410–444, https://doi.org/10.1080/10407790.2013.869102.
[128] D. Grapsas, R. Herbin, W. Kheriji, J.-C. Latche, An unconditionally stable staggered pressure correction scheme for the compressible Navier-Stokes equations, SMAI J. Comput. Math. 2 (2016) 51–97, https://doi.org/10.5802/smai-jcm.9.
[129] B. Klein, B. Müller, F. Kummer, M. Oberlack, A high-order discontinuous Galerkin solver for low Mach number flows, Int. J. Numer. Methods Fluids 81 (2016) 489–520, https://doi.org/10.1002/fld.4193.
[130] K.C. Ong, A. Chan, A pressure-based Mach-uniform method for viscous fluid flows, Int. J. Comput. Fluid Dyn. 30 (2016) 516–530, https://doi.org/10.1080/10618562.2016.1245417.
[131] C.N. Xiao, F. Denner, B.G.M. van Wachem, Fully-coupled pressure-based finite-volume framework for the simulation of fluid flows at all speeds in complex geometries, J. Comput. Phys. 346 (2017) 91–130, https://doi.org/10.1016/j.jcp.2017.06.009.
[132] X. Zhang, J.D. Chung, C.R. Kaplan, E.S. Oran, The barely implicit correction algorithm for low-Mach-number flows, Comput. Fluids 175 (2018) 230–245, https://doi.org/10.1016/j.compfluid.2018.08.019.
[133] Y. Moguen, P. Bruel, E. Dick, A combined momentum-interpolation and advection upstream splitting pressure-correction algorithm for simulation of convective and acoustic transport at all levels of Mach number, J. Comput. Phys. 384 (2019) 16–41, https://doi.org/10.1016/j.jcp.2019.01.029.
[134] B. Xie, X. Deng, S. Liao, High-fidelity solver on polyhedral unstructured grids for low-Mach number compressible viscous flow, Comput. Methods Appl. Mech. Eng. 357 (2019) 112584, https://doi.org/10.1016/j.cma.2019.112584.
[135] K. Yang, T. Aoki, Weakly compressible Navier-Stokes solver based on evolving pressure projection method for two-phase flow simulations, J. Comput. Phys. 431 (2021) 110113, https://doi.org/10.1016/j.jcp.2021.110113.
[136] Y. Cang, L. Wang, An improved fractional-step method on co-located unstructured meshes for weakly compressible flow simulations, Comput. Fluids 253 (2023) 105775, https://doi.org/10.1016/j.compfluid.2022.105775.
[137] R. Klein, Semi-implicit extension of a Godunov-type scheme based on low Mach number asymptotics I: one-dimensional flow, J. Comput. Phys. 121 (1995) 213–237, https://doi.org/10.1016/S0021-9991(95)90034-9.
[138] T. Schneider, N. Botta, K.J. Geratz, R. Klein, Extension of finite volume compressible flow solvers to multi-dimensional, variable density zero Mach number flows, J. Comput. Phys. 155 (1999) 248–286, https://doi.org/10.1006/jcph.1999.6327.
[139] R. Klein, N. Botta, T. Schneider, C.D. Munz, S. Roller, A. Meister, L. Hoffmann, T. Sonar, Asymptotic adaptive methods for multi-scale problems in fluid mechanics, J. Eng. Math. 39 (2001) 261–343, https://doi.org/10.1023/A:1004844002437.
[140] C.-D. Munz, S. Roller, R. Klein, K.J. Geratz, The extension of incompressible flow solvers to the weakly compressible regime, Comput. Fluids 32 (2003) 173–196, https://doi.org/10.1016/S0045-7930(02)00010-5.
[141] J.H. Park, C.-D. Munz, Multiple pressure variables methods for fluid flow at all Mach numbers, Int. J. Numer. Methods Fluids 49 (2005) 905–931, https://doi.org/10.1002/fld.1032.
[142] M. Boger, F. Jaegle, B. Weigand, C.-D. Munz, A pressure-based treatment for the direct numerical simulation of compressible multi-phase flow using multiple pressure variables, Comput. Fluids 96 (2014) 338–349, https://doi.org/10.1016/j.compfluid.2014.01.029.
[143] J. Guerra, B. Gustafsson, A numerical method for incompressible and compressible flow problems with smooth solutions, J. Comput. Phys. 63 (1986) 377–397, https://doi.org/10.1016/0021-9991(86)90200-7.
[144] B. Gustafsson, Unsymmetric hyperbolic systems and the Euler equations at low Mach numbers, J. Sci. Comput. 2 (1987) 123–136, https://doi.org/10.1007/BF01061482.
[145] M. Dumbser, V. Casulli, A conservative, weakly nonlinear semi-implicit finite volume scheme for the compressible Navier-Stokes equations with general equation of state, Appl. Math. Comput. 272 (2016) 479–497, https://doi.org/10.1016/j.amc.2015.08.042.
[146] M. Ioriatti, M. Dumbser, R. Loubere, A staggered semi-implicit discontinuous Galerkin scheme with a posteriori subcell finite volume limiter for the Euler equations of gasdynamics, J. Sci. Comput. 83 (2020) 27, https://doi.org/10.1007/s10915-020-01209-w.
[147] M. Tavelli, M. Dumbser, A pressure-based semi-implicit space-time discontinuous Galerkin method on staggered unstructured meshes for the solution of the compressible Navier-Stokes equations at all Mach numbers, J. Comput. Phys. 341 (2017) 341–376, https://doi.org/10.1016/j.jcp.2017.03.030.
[148] W. Boscheri, M. Tavelli, High order semi-implicit schemes for viscous compressible flows in 3D, Appl. Math. Comput. 434 (2022) 127457, https://doi.org/10.1016/j.amc.2022.127457.
[149] W. Boscheri, M. Dumbser, M. Ioriatti, I. Peshkov, E. Romenski, A structure-preserving staggered semi-implicit finite volume scheme for continuum mechanics, J. Comput. Phys. 424 (2021) 109866, https://doi.org/10.1016/j.jcp.2020.109866.
[150] S. Parada, R. Codina, J. Baiges, Development of an algebraic fractional step scheme for the primitive formulation of the compressible Navier-Stokes equations, J. Comput. Phys. 433 (2021) 110017, https://doi.org/10.1016/j.jcp.2020.110017.
[151] A. Hennink, M. Tiberga, D. Lathouwers, A pressure-based solver for low-Mach number flow using a discontinuous Galerkin method, J. Comput. Phys. 425 (2021) 109877, https://doi.org/10.1016/j.jcp.2020.109877.
[152] A. Bermudez, S. Busto, M. Dumbser, J. Ferrin, L. Saavedra, M. Vazquez-Cendon, A staggered semi-implicit hybrid FV/FE projection method for weakly compressible flows, J. Comput. Phys. 421 (2020) 109743, https://doi.org/10.1016/j.jcp.2020.109743.
[153] S. Busto, L. Rio-Martin, M.E. Vazquez-Cendon, M. Dumbser, A semi-implicit hybrid finite volume/finite element scheme for all Mach number flows on staggered unstructured meshes, Appl. Math. Comput. 402 (2021) 126117, https://doi.org/10.1016/j.amc.2021.126117.
[154] S. Busto, M. Dumbser, L. Rio-Martin, An arbitrary-Lagrangian-Eulerian hybrid finite volume/finite element method on moving unstructured meshes for the Navier-Stokes equations, Appl. Math. Comput. 437 (2023) 127539, https://doi.org/10.1016/j.amc.2022.127539.
[155] Y. Kanarska, T. Dunn, L. Glascoe, K. Lundquist, C. Noble, Semi-implicit method to solve compressible multiphase fluid flows without acoustic time step restrictions, Comput. Fluids 210 (2020) 104651, https://doi.org/10.1016/j.compfluid.2020.104651.
[156] A. Urbano, M. Bibal, S. Tanguy, A semi implicit compressible solver for two-phase flows of real fluids, J. Comput. Phys. 456 (2022) 111034, https://doi.org/10.1016/j.jcp.2022.111034.
[157] B. Re, R. Abgrall, A pressure-based method for weakly compressible two-phase flows under a Baer-Nunziato type model with generic equations of state and pressure and velocity disequilibrium, Int. J. Numer. Methods Fluids 94 (2022) 1183–1232, https://doi.org/10.1002/fld.5087.
[158] G. Sirianni, B. Re, R. Abgrall, A. Guardone, Momentum weighted interpolation for unsteady weakly compressible two-phase flows on unstructured meshes, J. Comput. Appl. Math. 428 (2023) 115209, https://doi.org/10.1016/j.cam.2023.115209.
[159] G. Dal Maso, P. Le Floch, F. Murat, Definition and weak stability of nonconservative products, J. Math. Pures Appl. 74 (1995) 483–548.
[160] C. Chalons, Path-conservative in-cell discontinuous reconstruction schemes for non conservative hyperbolic systems, Commun. Math. Sci. 18 (2020) 1–30, https://doi.org/10.4310/CMS.2020.v18.n1.a1.
[161] R. Abgrall, S. Karni, A comment on the computation of non-conservative products, J. Comput. Phys. 229 (2010) 2759–2763, https://doi.org/10.1016/j.jcp.2009.12.015.
[162] E.F. Toro, Riemann Solvers and Numerical Methods for Fluid Dynamics. A Practical Introduction, 3rd ed., Springer, Dordrecht, Heidelberg, London, New York, 2009.
[163] F. Setzwein, P. Ess, P. Gerlinger, An implicit high-order k-exact finite-volume approach on vertex-centered unstructured grids for incompressible flows, J. Comput. Phys. 446 (2021) 110629, https://doi.org/10.1016/j.jcp.2021.110629.
[164] Y. Loukili, A. Soulaimani, Numerical tracking of shallow water waves by the unstructured finite volume WAF approximation, Int. J. Comput. Methods Eng. Sci. Mech. 8 (2007) 75–88, https://doi.org/10.1080/15502280601149577.

[165] R. Ata, S. Pavan, S. Khelladi, E.F. Toro, A weighted average flux (WAF) scheme applied to shallow water equations for real-life applications, Adv. Water Resour. 62 (2013) 155–172, https://doi.org/10.1016/j.advwatres.2013.09.019.
[166] W. Speares, E.F. Toro, A high resolution algorithm for time dependent shock dominated problems with adaptive mesh refinement, Z. Flugwiss. Weltraumforsch. 19 (1995) 267–281.
[167] E.F. Toro, A linearized Riemann solver for the time-dependent Euler equations of gas dynamics, Proc. R. Soc. A 434 (1991) 683–693, https://doi.org/10.1098/rspa.1991.0121.
[168] P. Lax, B. Wendroff, Systems of conservation laws, Commun. Pure Appl. Math. 13 (1960) 217–237, https://doi.org/10.1002/cpa.3160130205.
[169] A. Lerat, Une classe de schemas aux differences implicites pour les systemes hyperboliques de lois de conservation, C. R. Acad. Sci. Paris (1979) 1033–1036.
[170] A. Lerat, Implicit methods of second-order accuracy for the Euler equations, AIAA J. 23 (1985) 33–40, https://doi.org/10.2514/3.8868.
[171] C. Hirsch, Numerical Computation of Internal and External Flows, Volume 2: Computational Methods for Inviscid and Viscous Flows, John Wiley & Sons, Chichester, New York, Brisbane, Toronto, Singapore, 1984.
[172] J. Stoer, R. Burlisch, Introduction to Numerical Analysis, 2nd ed., Springer Science+Business Media, LLC, New York, 1993.
[173] C.R. Johnson, Positive definite matrices, Am. Math. Mon. 77 (1992) 259–264, https://doi.org/10.1080/00029890.1970.11992465.
[174] H.A. van der Vorst, Bi-CGSTAB: A fast and smoothly converging variant of Bi-CG for the solution of nonsymmetric linear systems, SIAM J. Sci. Stat. Comput. 13 (1992) 631–644, https://doi.org/10.1137/0913035.
[175] C. Hirsch, Numerical Computation of Internal and External Flows, Volume 1: Fundamentals of Numerical Discretization, John Wiley & Sons, Chichester, New York, Brisbane, Toronto, Singapore, 1988.
[176] R.D. Richtmeyer, K.W. Morton, Difference Methods for Initial-Value Problems, 2nd ed., Interscience Tracts in Pure and Applied Mathematics, vol. 4, Interscience Publishers, New York, Chichester, Brisbane, Toronto, 1967.
[177] S.K. Godunov, I. Bohachevsky, Finite difference method for numerical computation of discontinuous solutions of the equations of fluid dynamics, Mat. Sb. 47 (89) (1959) 271–306.
[178] V. Venkatakrishnan, On the accuracy of limiters and convergence to steady state solutions, in: Proceedings of 31st Aerospace Sciences Meeting, 1993, AIAA93-0880.
[179] G. Sod, A survey of several finite difference methods for systems of nonlinear hyperbolic conservation laws, J. Comput. Phys. 27 (1978) 1–31, https://doi.org/10.1016/0021-9991(78)90023-2.
[180] C.-D. Munz, M. Dumbser, S. Roller, Linearized acoustic perturbation equations for low Mach number flow with variable density and temperature, J. Comput. Phys. 224 (2007) 352–364, https://doi.org/10.1016/j.jcp.2007.02.022.
[181] U. Ghia, K. Ghia, C. Shin, High-Re solutions for incompressible flow using the Navier-Stokes equations and a multigrid method, J. Comput. Phys. 48 (1982) 387–411, https://doi.org/10.1016/0021-9991(82)90058-4.
[182] H. Schlichting, G. Gersten, Boundary Layer Theory, 8th ed., Springer, Berlin, Heidelberg, New York, Barcelona, Hong Kong, London, Milan, Paris, Singapore, Tokyo, 2000.
[183] J.D. Anderson Jr., Fundamentals of Aerodynamics, 6th ed., McGraw-Hill Education, 2017.
[184] P.M. Morse, K.U. Ingard, Theoretical Acoustics, Princeton University Press, Princeton, New Jersey, 1986.
[185] S. Roux, G. Lartigue, T. Poinsot, U. Meier, C. Berat, Studies of mean and unsteady flow in a swirled combustor using experiments, acoustic analysis, and large eddy simulations, Combust. Flame 141 (2005) 40–54, https://doi.org/10.1016/j.combustflame.2004.12.007.
[186] F. Nicoud, F. Ducros, Subgrid-scale stress modelling based on the square of the velocity gradient tensor, Flow Turbul. Combust. 62 (1999) 183–200, https://doi.org/10.1023/A:1009995426001.